Generated using the official AMS LaTeX template v6.1

Investigating the strength and variability of El Niño Southern Oscillation teleconnections to hydroclimate and maize yields in southern and East Africa

Benjamin I Cook[1,2] and Weston Anderson[3,4] and Kimberly Slinski[3,4] and Shraddhanand Shukla[5] and Amy McNally[4]

[1]NASA Goddard Institute for Space Studies, New York, New York, USA
[2]Division of Ocean and Climate Physics, Lamont-Doherty Earth Observatory, Palisades, New York, USA
[3]Earth System Science Interdisciplinary Center, University of Maryland, College Park, Maryland, USA
[4]NASA Goddard Space Flight Center, Greenbelt, Maryland, USA
[5]Climate Hazards Center, University of California-Santa Barbara, Santa Barbara, California, USA

Corresponding author: Benjamin I Cook, benjamin.i.cook@nasa.gov

ABSTRACT: The state of the El Niño Southern Oscillation (ENSO) is critical for seasonal climate forecasts, but recent events diverged substantially from expectations in many regions, including Sub-Saharan Africa where seasonal forecasts are critical tools for addressing food security. Here, we evaluate 39 years (1982–2020) of data on hydroclimate, leaf area index, and maize yields to investigate the strength of ENSO teleconnections in southern and East Africa. Teleconnections to precipitation, soil moisture, and leaf area index are generally stronger during ENSO phases that cause drought conditions (El Niño in southern Africa and La Niña in East Africa), with seasonality that aligns well with the maize growing seasons. Within maize growing areas, however, ENSO teleconnections to hydroclimate and vegetation are generally weaker compared to the broader geographic regions, especially in East Africa. There is also little evidence that the magnitude of the ENSO event affects the hydroclimate or vegetation response in these maize regions. Maize yields in Kenya, Malawi, South Africa, and Zimbabwe all correlate significantly with hydroclimate and leaf area index, with South Africa and Zimbabwe showing the strongest and most consistent yield responses to ENSO events. Our results highlight the chain of causality from El Niño and La Niña forcing of regional anomalies in hydroclimate to vegetation health and maize yields in southern and East Africa. The large spread across individual ENSO events, however, underscores the limitations of this climate mode for seasonal climate prediction in the region, and the importance of finding additional sources of skill for improving climate and yield forecasts.

1. Introduction

The state of the El Niño Southern Oscillation (ENSO) system is one the most important sources of skill in seasonal climate forecasts (Goddard et al. 2001). This is because cold (La Niña) and warm (El Niño) ENSO states, and their regional climate impacts, can be skillfully predicted at least several months in advance (Barnston et al. 2019; Goddard et al. 2001; Lenssen et al. 2020). As such, ENSO events often have major implications for crop yields and malnutrition (Anttila-Hughes et al. 2021; Guimarães Nobre et al. 2019; Sazib et al. 2020; Ubilava and Abdolrahimi 2019), highlighting the value of using ENSO-informed forecasts to monitor and predict changes in food security (Guimarães Nobre et al. 2019; Goddard and Dilley 2005). The Famine Early Warning Systems Network (FEWS NET), for example, uses seasonal climate and ENSO forecasts, with other information, to monitor and forecast levels of food insecurity in many developing regions around the world (Backer and Billing 2021; Funk et al. 2019; Ross et al. 2009). This includes countries in Central Asia, Sub-Saharan Africa, and Central America, developing regions often dependent on international aid when food insecurity arises.

Despite their value for seasonal climate predictions, however, there have been several recent incidents where seasonal climate forecasts diverged significantly from what was expected given the ENSO state at the time. One of the more notable occurrences in the last decade was the 2015/16 El Niño, at the time the strongest El Niño event in 36 years (Kogan and Guo 2017). Despite the magnitude of this El Niño event, however, regional hydroclimate and food security conditions deviated substantially from forecasts in regions like East Africa (Choularton and Krishnamurthy 2019; Krishnamurthy et al. 2020), the western United States (Jong et al. 2018; Paek et al. 2017), and Peru and Ecuador (Cai et al. 2020). Weaker than expected teleconnections during some ENSO events can often be traced to dynamical differences in how the events evolve (Jong et al. 2018; Paek et al. 2017). Teleconnections can also be affected by other sources of variability in the climate system, including other climate modes (Ashcroft et al. 2016), internal atmospheric variability (Deser et al. 2017), and even ocean temperatures in other basins (Giannini et al. 2004). There are also large uncertainties regarding how well the classic ENSO teleconnections to precipitation translate through the land surface (e.g., soil moisture), and the implications this may have for vegetation health and crop yields. Studies that have addressed this topic have often focused on relatively short time periods (Anyamba et al. 2018, 2002; Sazib et al. 2020) with a limited number of ENSO events, potentially under-sampling important variability in the climate system. Sazib et al. (2020), for example, found strong associations between ENSO states and soil moisture and crop yields in southern and East Africa, but only used ten years for their analysis (2010–2019) and did not explicitly highlight the extent to which ENSO events may differ from each other.

Here, we build upon and extend previous work by using nearly 40 years of observations to investigate and quantify the strength of El Niño and La Niña impacts on climate, vegetation, and crop yields in southern and East Africa. These are regions with major food security concerns, and where the impacts of individual ENSO events have been well documented in the past. For our analyses, we primarily focus on the major cropping regions for maize, the single most important food crop in the region for countries that depend upon food imports to meet their nutritional needs (e.g., Zimbabwe) or serve as a major exporter supporting other countries in the regional food system (e.g., South Africa). Further, the extended period of observations we use greatly expands the number of ENSO events sampled compared to previous analyses (e.g., Sazib et al. 2020), allowing us to look in more detail at differences across events. We focus on the following research questions: (1) Are ENSO impacts on hydroclimate and vegetation in southern and East Africa equally expressed for El Niño and La Niña events?; (2) How strongly does the magnitude of ENSO forced regional hydroclimate and vegetation impacts scale with event strength?; (3) How does the seasonal evolution of climate and vegetation compare across some of the strongest events in recent decades (1997/98 vs the 2015/16 El Niño; 1998/99 vs 2010/11 La Niña)?; and (4) How sensitive are country-level maize yields to climate variability and ENSO in these regions?

2. Materials and Methods

a. Defining ENSO Events

We identifed El Niño and La Niña events using December-January-February (DJF) values of the the Oceanic Niño Index (ONI) from the Climate Prediction Center (CPC) (`https://origin.cpc.ncep.noaa.gov/products/analysis_monitoring/ensostuff/ONI_v5.php`). The ONI uses sea surface temperatures (SSTs) averaged over the Niño 3.4 region (5°N–5°S, 120°W–170°W). We defined El Niño events when 3-month DJF running mean Niño 3.4 SSTs meet or exceed +0.5^{o}C and La Niña conditions when the 3-month DJF running mean values are equal to or colder than

-0.5^oC. Based on our definition, we identified 14 El Niño events and 15 La Niña events over the 39 year study period of 1982–2020 (Table 1).

Table 1. List of ENSO events analyzed in this study.

El Niño	La Niña
1982/1983, 1986/1987, 1987/1988, 1991/1992, 1994/1995, 1997/1998, 2002/2003, 2004/2005, 2006/2007, 2009/2010, 2014/2015, 2015/2016, 2018/2019, 2019/2020	1983/1984, 1984/1985, 1985/1986, 1988/1989, 1995/1996, 1996/1997, 1998/1999, 1999/2000, 2000/2001, 2005/2006, 2007/2008, 2008/2009, 2010/2011, 2011/2012, 2017/2018

For our analyses, we consider climate responses across the full life cycle of these ENSO events, from at least 6 months prior to the event peak and through at least the 6 months following. ENSO events typically develop over the course of an entire calendar year, and it is well established that some ENSO teleconnections are strongest during the months leading up to, or following, the event peak in the boreal winter (Yeh et al. 2018). This is because the atmospheric responses to ENSO SSTs that drive various regional teleconnections can get stimulated before the ENSO events reach their peak, or may lag behind as the atmosphere adjusts to the change in SST boundary forcing. For example, El Niño events are most strongly associated with reduced Indian monsoon rainfall in the summer and fall prior to the winter event peak (Kumar et al. 2006). Similarly, the strongest correlations between ENSO and precipitation over northeast Brazil occur in the spring following the winter peak (Rodrigues et al. 2011).

b. Precipitation and Soil Moisture Data

Precipitation and soil moisture data are taken from the FEWS NET Land Data Assimilation System (FLDAS) (McNally et al. 2017), part of NASA's Land Information System framework. FLDAS is a suite of global land surface model simulations from 1982 through the present, forced by precipitation from the Climate Hazards Group Infrared Precipitation with Station (CHIRPS) precipitation forcing dataset (Funk et al. 2015) and other meteorological forcings from the NOAA Global Data Assimilation System (GDAS) (Derber et al. 1991) and NASA's Modern Era Reanalysis for Research and Applications version 2 (MERRA-2) (Bosilovich et al. 2015). From FLDAS, we analyze the CHIRPS data and the 200 centimeter soil moisture from the NOAH model. While the soil moisture is modeled, previous analyses have confirmed that the high quality of the CHIRPS precipitation inputs produces modeled soil moisture estimates that compare favorably with observations (Jung et al. 2019; McNally et al. 2016, 2017).

To test the sensitivity of our analyses to dataset choices, we also use precipitation from the Global Precipitation Climatology Centre (GPCC) (Schneider et al. 2022) and root zone soil moisture (top 1-3 meters, depending on grid cell vegetation) from the Global Land Evaporation Amsterdam Model (GLEAM) (Martens et al. 2017; Miralles et al. 2011). Unlike FLDAS, GLEAM root zone soil moisture is not solely a product derived from a model driven by atmospheric forcing (e.g., precipitation). GLEAM uses a Kalman filter to directly assimilate satellite observations of surface soil moisture from version 6.2 of the ESA-CCI product (Dorigo et al. 2017; Gruber et al. 2017) into the top soil layer in the model, providing an additional constraint on GLEAM estimates compared to products (like FLDAS) that are solely derived from atmospheric inputs.

c. Leaf Area Index Data

Monthly average values of leaf Area Index (LAI) data are taken from version 3 of the GLOBMAP dataset (Liu et al. 2012). GLOBMAP is a satellite based, global LAI dataset available at 8 km spatial resolution. It is constructed by merging LAI from historical Advanced Very High Resolution Radiometer (AVHRR) (1981–2000; half month temporal availability) and Moderate Resolution Imaging Spectroradiometer (MODIS) sensors (2001–2020; 8-day temporal availability). As with precipitation and soil moisture, we compare results using GLOBMAP LAI against an alternative dataset, version 4g of the Global Inventory Modeling and Mapping Studies (GIMMS) LAI dataset (Cao et al. 2023).

d. Maize Cropping

Maize cropping regions were identified using the Best Available Crop Specific masks (BACS) from the Group on Earth Observations Global Agriculture Monitoring (GEOGLAM) Crop Monitor dataset (Becker-Reshef et al. 2023). These data were aggregated to a half degree resolution to match the resolution of other datasets used in our analysis. Any grid cell with greater than 1% harvested maize area was included in our analysis, producing the maize masks used for aggregating across southern and East Africa (Figure 1). We tested alternative thresholds for the masking at ≥ 0.0%, 0.1%, 2.0%, and 10% (Supplementary Figure 1). A threshold of 0.1% would include nearly every grid cell in many of our countries of interest (e.g., Zambia, Zimbabwe, Mozambique), most of

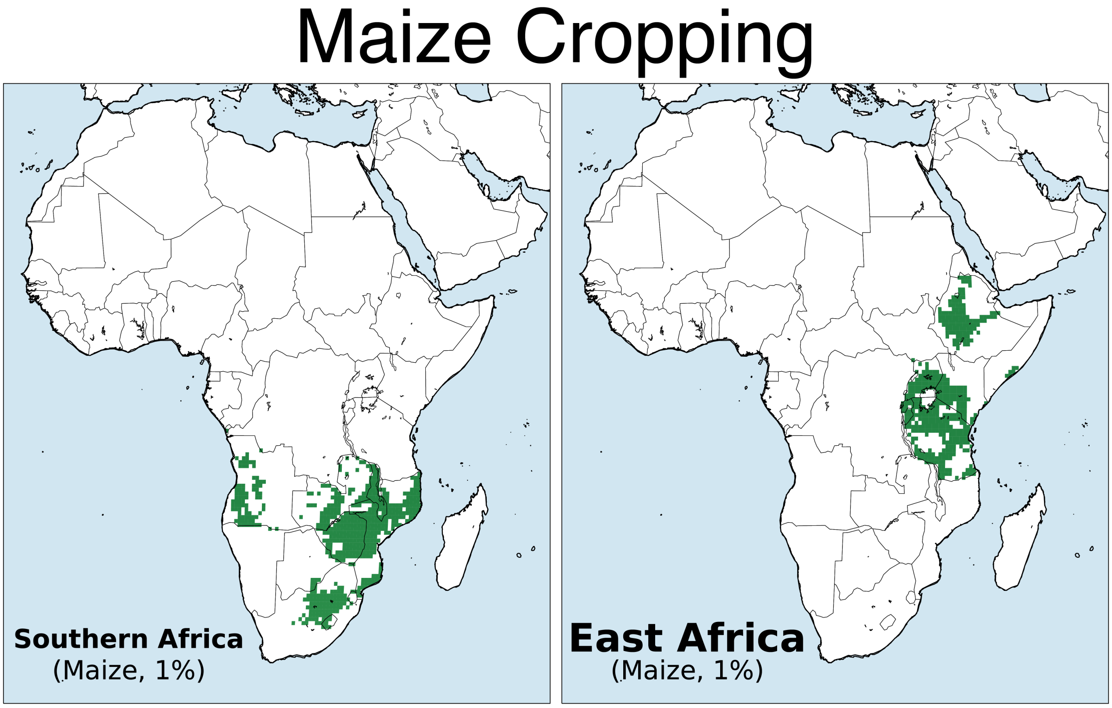

Fig. 1. Major maize cropping regions in southern Africa and East Africa, where at least 1% of grid cell area is planted for maize. Countries in our southern Africa region with substantial maize cropping include Angola, Zambia, Zimbabwe, Malawi, Mozambique, South Africa, and Lesotho. In East Africa, these include Kenya, Ethiopia, Tanzania, Uganda, Rwanda, and Burundi.

which are unlikely to be major production areas. A threshold of 10%, however, would leave virtually zero grid cells available in most of these countries. No grid cells in Ethiopia, for example, exceed this threshold. We therefore chose 1% as a compromise that allows for (1) reasonable sampling of grid cells for our regional and country-level averaging while (2) excluding areas that are likely not major production regions. Maize cropping seasons for each country (including planting and harvest periods), used to contextualize the country-level analyses of climate and maize yields, were taken from the International Production Assessment Division of the United States Department of Agriculture Foreign Agricultural Service (`https://ipad.fas.usda.gov/countrysummary/`).

e. Crop Yield Data

Crop yield data for Kenya, South Africa, Malawi, and Zimbabwe were taken from the FAOSTAT database (Food and Agriculture Organization of the United Nations 2023). These countries have

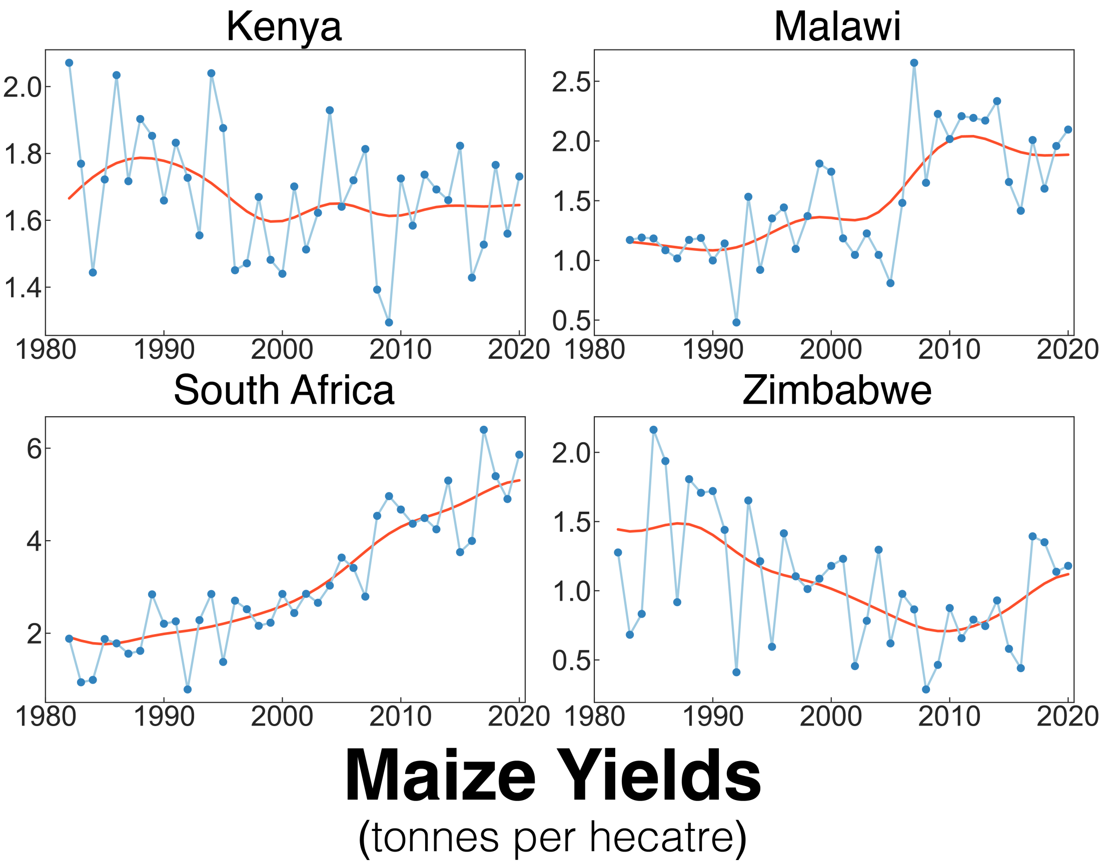

Fig. 2. Crop yields from the FAOSTAT database (blue lines) and the low-frequency Gaussian filter (orange lines) with a kernel density of three years used to estimate fractional yield anomalies for our analyses.

been previously identified as (1) having significant ENSO teleconnections to maize yields and (2) data of sufficient quality to identify such teleconnections. Crop yields are sensitive to a variety of factors aside from climate and weather variability, including fertilizer use, available technology, crop cultivars, and agricultural policies. As such, it is a well established best practice to remove long-term trends (e.g., by first differencing the data or differencing from a smoothed average) to isolate climate and weather signals in the crop yield data (e.g., Calderini and Slafer 1998; Lobell and Field 2007; Lobell and Tebaldi 2014), including in analyses of ENSO and crop yields (Anderson et al. 2019, 2023; Iizumi et al. 2014). For our analyses, we took the observed FAOSTAT crop yields (Figure 2, blue lines) and applied a low-frequency Gaussian filter (Figure 2, orange lines) with a kernel density of three years to calculate expected yields (i.e., the estimated yield attributable to management and technology). This resulting trend is similar to a nine-year running mean. We then calculated the crop yield anomalies as the difference between the observed and expected yields. Finally, we divided these anomalies by the expected yield to calculate the fractional yield anomaly (in units of fraction of expected yield) that is used in our analyses.

f. Analyses

Prior to our analyses, all precipitation, soil moisture, and LAI data for each month were linearly detrended over the full period of study (1982–2020). The resulting residual anomalies were then superimposed on the long-term mean calculated over the same period. Overall, detrending had negligible effects on our results and conclusions (not shown). For the regional and country-level analyses, we calculated area-weighted averages using the southern and East Africa maize cropping masks in Figure 1, preserving the original units of the data.

To assess the strength of the ENSO teleconnections at each grid cell, we calculated the "anomaly sign consensus" for the El Niño and La Niña composite maps, defined as the fraction of events with an anomaly sign consistent with the sign of the composite mean anomaly. This indicator has been used in other studies and reports (e.g., Dirmeyer et al. 2013) and we apply it here for two reasons. First, it is highly interpretable and relatively simple to implement and understand, making no assumptions about the underlying data structure, an advantage given the limited sampling of ENSO events available over our period of analysis. Second, it is a highly relevant metric from the perspective of seasonal climate predictions, where there is strong interest in accurate predictions of below or above average anomalies.

To determine the "significance" of the anomaly sign consensus values, we modified the approach of Dirmeyer et al. (2013). First, we generated 10,000 random series sampled from (-1, +1) with lengths equal to the number of El Niño (n=14) or La Niña (n=15) events. This null hypothesis assumes, as in Dirmeyer et al. (2013), equal probabilities of either anomaly sign. We then processed each time series identically to the original data (linearly detrending and recentering on zero mean) and then calculated the anomaly sign consensus. From these 10,000 anomaly sign consensus values, we calculated the 95th percentile, and used this as our significance threshold. For both phases, this threshold was 10 events, corresponding to approximately 71% and 67% of El Niño and La Niña events, respectively. We also conducted a two-sample Wilcoxon rank sum test (one sided, $p \leq 0.05$ significance level), comparing (at each grid cell) differences between median anomalies during all El Niño and all La Niña years. For both the anomaly sign consensus and Wilcoxon tests, we apply hatching to mask areas with insignificant results.

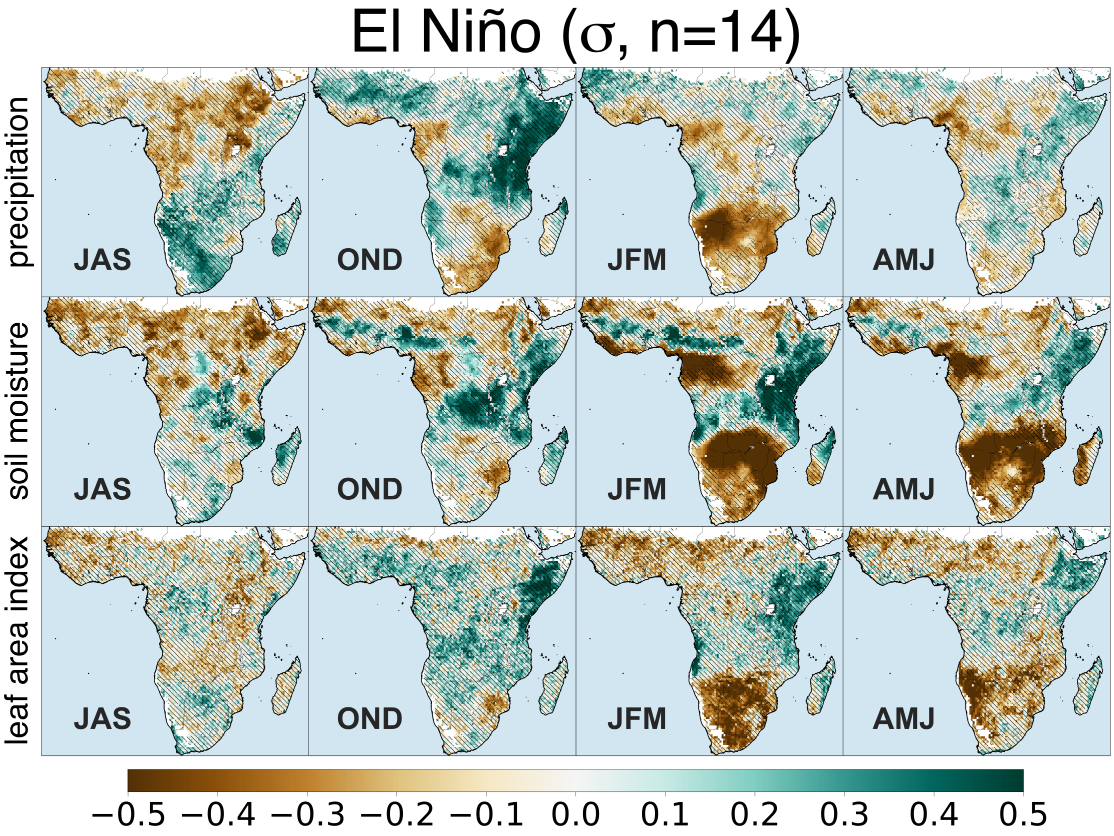

FIG. 3. Composite average standardized anomalies of precipitation, soil moisture (200 cm), and leaf area index during El Niño (n=14) events from 1982–2020. Areas where at least 10 of the 14 (approximately 71%) El Niño events have the same sign of response as the composite average are considered regions with significant agreement in the anomaly sign consensus metric. All other areas are hatched. July-August-September (JAS) and October-November-December (OND) anomalies are taken from the year corresponding with the development of the El Niño event (e.g., 1997), while all other seasons are taken from the following year (e.g., 1998).

3. Results

a. El Niño Composite Anomalies

Beginning in July-August-September (JAS) of the preceding calendar year, El Niño events are associated with negative precipitation anomalies across Ethiopia, Sudan, South Sudan, and western Kenya (Figure 3). The precipitation response to El Niño subsequently switches sign to positive across most of East Africa during the following "short rains" of October-November-December (OND). These somewhat complex ENSO teleconnection patterns are well established in the literature (Kiflie and Tao 2020; Korecha and Barnston 2007; Nicholson and Kim 1997; Nicholson 2017; Palmer et al. 2023; Vashisht et al. 2021). In the northern Greater Horn of Africa (GHA) region, which receives the majority of its rainfall in JAS, precipitation is reduced during El Niño and increased during La Niña. By contrast, in the equatorial region of GHA (including Eastern Kenya and Somalia) October-December rainfall (one of the two key bi-modal seasons) anomalies are wetter than normal during El Niño and drier than normal during La Niña, and additionally modulated by the Indian Ocean Dipole.

Composite JAS precipitation anomalies during El Niño are positive over southern Africa and negative during OND across most of South Africa and the southern parts of Mozambique and Zimbabwe. These southern Africa precipitation deficits intensify and expand across most of the region in January-February-March (JFM). Notably, and regardless of the absolute magnitude of the composite mean anomaly, the anomaly sign consensus is generally more significant for drought anomalies compared to wetter than average conditions. For example, despite strong and widespread positive mean precipitation anomalies during El Niño across East Africa in OND, there is substantial hatching (indicating the anomaly sign consensus is not significant) across these areas. This contrasts with the drought response to El Niño in southern Africa in OND and JFM, which is significant across most areas with large precipitation deficits.

Soil moisture and LAI responses in both regions are consistent with the sign of the precipitation responses. In East Africa, high precipitation in OND causes positive soil moisture anomalies that largely persist through JFM and April-May-June (AMJ). The widespread hatching, however, highlights the large spread across El Niño events in this response. LAI anomalies follow the same patterns as the soil moisture in East Africa, though these responses are even weaker in terms of intensity, spatial extent, and significance of the anomaly sign consensus compared to the East Africa soil moisture anomalies. In southern Africa, widespread and intense soil moisture drying occurs during El Niño in JFM and AMJ. Negative LAI anomalies align closely with these soil moisture responses, though the LAI response is most widespread during JFM and mostly isolated to Namibia and Angola during the AMJ transition into the dry season. As with precipitation, these drought associated soil moisture and LAI anomalies show stronger agreement across events compared to anomalies associated with wetter conditions.

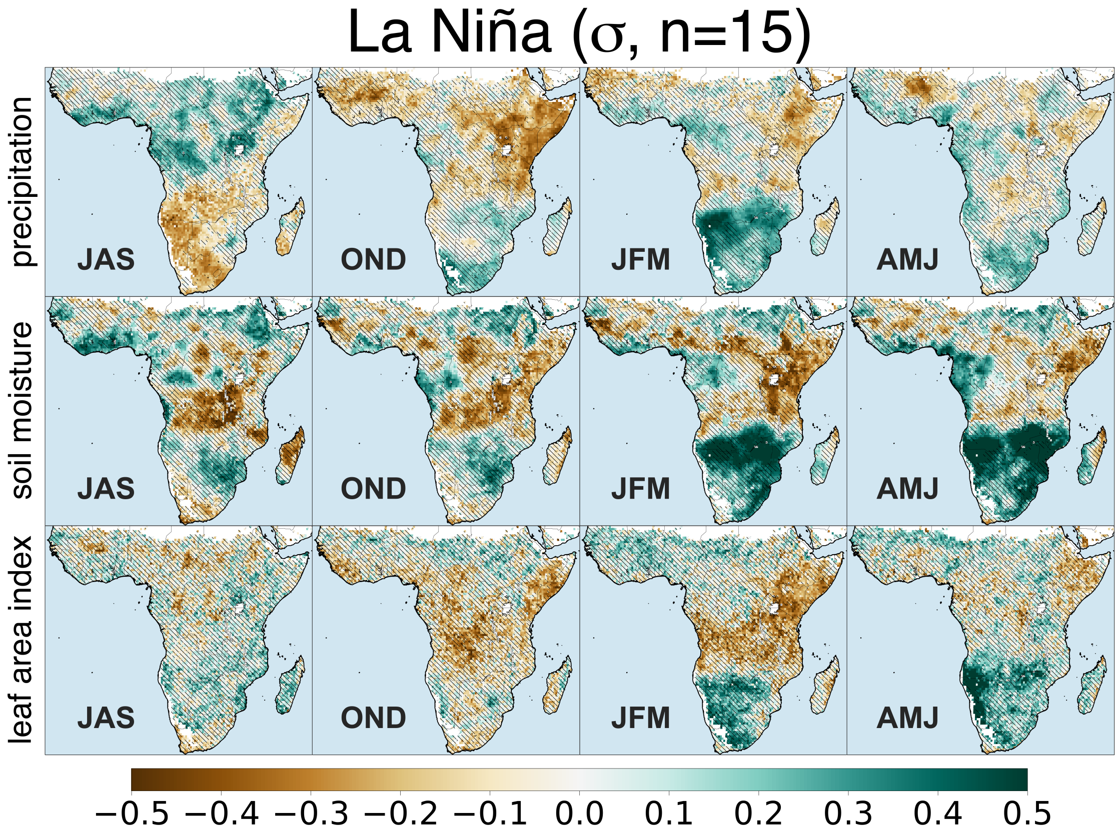

FIG. 4. Composite average standardized anomalies of precipitation, soil moisture (200 cm), and leaf area index during La Niña (n=15) events from 1982–2020. Areas where at least 10 of the 15 (approximately 67%) La Niña events have the same sign of response as the composite average are considered regions with significant agreement in the anomaly sign consensus metric. All other areas are hatched. July-August-September (JAS) and October-November-December (OND) anomalies are taken from the year corresponding with the development of the La Niña event (e.g., 1998), while all other seasons are taken from the following year (e.g., 1999).

b. La Niña Composite Anomalies

The composite average anomalies during La Niña over Sub-Saharan Africa are generally of opposite sign compared to El Niño (Figure 4), with a similar tendency towards higher agreement across events in the sign of the anomaly in regions with drier conditions. During JAS of the preceding year, La Niña causes above normal precipitation across large areas of East Africa and widespread precipitation deficits over southern Africa. This is the dry season over southern Africa, and these ostensibly large standardized anomalies represent small declines in absolute precipitation. La Niña causes widespread and intense precipitation deficits during the OND short rains over East Africa and increased precipitation in southern Africa, especially during JFM.

As during El Niño events, soil moisture and LAI responses lag the La Niña precipitation anomalies. In East Africa, soil moisture declines begin with the short rains deficits in OND and persist through JFM and AMJ, especially over Kenya, Tanzania, and the southern parts of Sudan and Somalia. LAI declines associated with this drying are strongest in JFM, matching closely with the areas of most significant soil moisture deficits. Positive soil moisture anomalies in southern Africa are most widespread during JFM and AMJ. Strong positive LAI anomalies are concurrent with the largest positive soil moisture anomalies, though the largest and most significant anomalies are centered over Namibia and the western part of southern Africa.

Areas of significant differences in the median anomalies between the two ENSO phases (El Niño minus La Niña; Figure 5) match well with areas with significant anomaly sign consensus (Figures 3 and 4), clear examples being precipitation in east Africa during OND and southern Africa during JFM. However, looking solely at these results obfuscates the asymmetric nature of the teleconnections highlighted by the anomaly sign consensus. For example, while Figure 5 shows that OND precipitation is significantly higher during El Niño than La Niña across much of East Africa, the anomaly sign consensus results demonstrate the stronger and more consistent nature of the La Niña drought teleconnection.

We find very similar results results from the anomaly sign consensus and Wilcoxon ranksum tests using the alternative datasets (GPCC precipitation, GLEAM root zone soil moisture, and GIMMS 4g LAI) (Supplementary Figures 2–4). This includes the overall tendency for more stronger anomaly sign consensus during drought teleconnections, and similar anomaly magnitudes in the event composites. Overall, this suggests that the conclusions from our analyses so far are largely insensitive to the datasets chosen.

c. ENSO Seasonality in Maize Regions

Anomalies of precipitation, soil moisture, and LAI averaged over maize growing regions during ENSO events in southern (Figure 6) and East (Figure 7) Africa are consistent with the composite

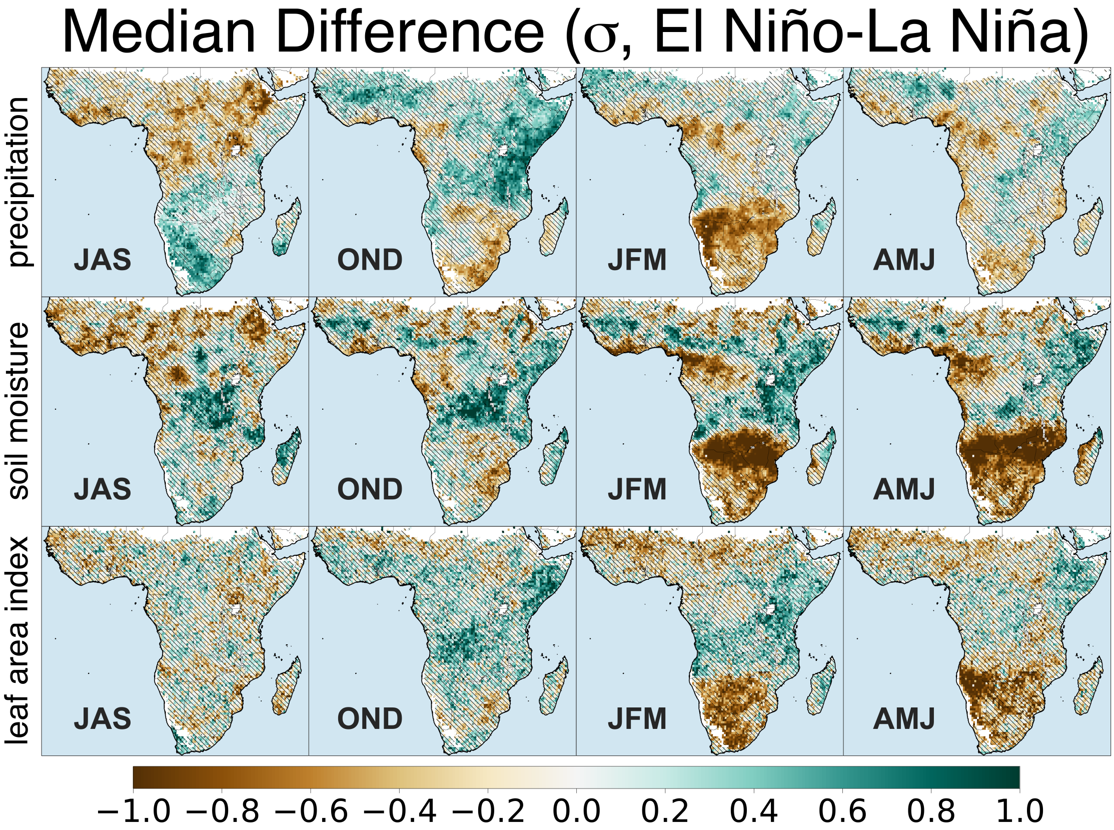

FIG. 5. Differences in median standardized anomalies of precipitation, soil moisture (200 cm), and leaf area index between ENSO phases (El Niño minus La Niña). Significance is assessed using a two sample Wilcoxon-Rank sum test (one sided, $p \leq 0.05$), with insignificant areas indicated by the hatching. July-August-September (JAS) and October-November-December (OND) anomalies are taken from the year corresponding with the development of the El Niño or La Niña event, while all other seasons are taken from the following year.

anomaly maps in Figures 3–4. Further, significant differences (two sample Wilcoxon Rank Sum test; significance levels indicated by asterisks in the figure panels) between El Niño and La Niña events can be found in these variables for several seasons, also consistent with the composite event median comparisons in Figure 5.

In maize regions of southern Africa (Figure 6), precipitation is significantly (indicated by the asterisks; see figure caption for details) drier during El Niño events compared to La Niña in JFM, the latter half of the wet season, driving the significantly reduced soil moisture in JFM and AMJ. LAI responses lag the precipitation and soil moisture anomalies, with significantly lower median LAI during El Niño in AMJ. In East Africa (Figure 7), precipitation is significantly lower in JAS

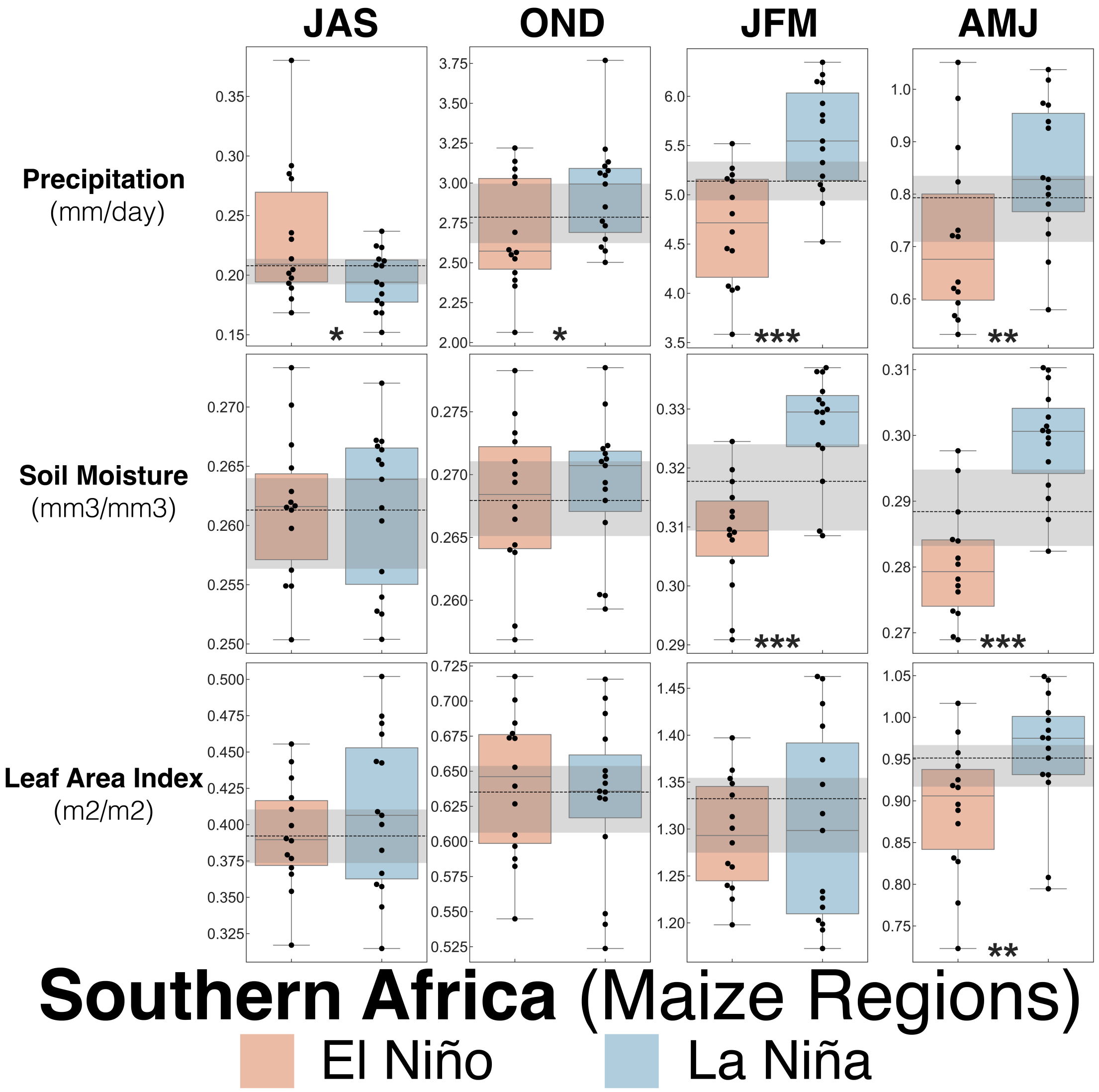

FIG. 6. Box and swarm plots of precipitation, soil moisture (200 cm), and LAI during El Niño and La Niña over southern Africa. Each observation is the area-weighted average during the specified season over the maize cropping regions of southern Africa identified in Figure 1. Grey shading indicates the central tercile of anomalies from all years in our datasets (1982–2020). As previously noted, July-August-September (JAS) and October-November-December (OND) anomalies are taken from the year corresponding with the peak in the ENSO event, while other seasons are from the following year. Asterisks indicate significance levels from a two-sample Wilcoxon rank sum test comparing El Niño and La Niña distributions: $*p \leq 0.10$, $**p \leq 0.05$, and $***p \leq 0.01$.

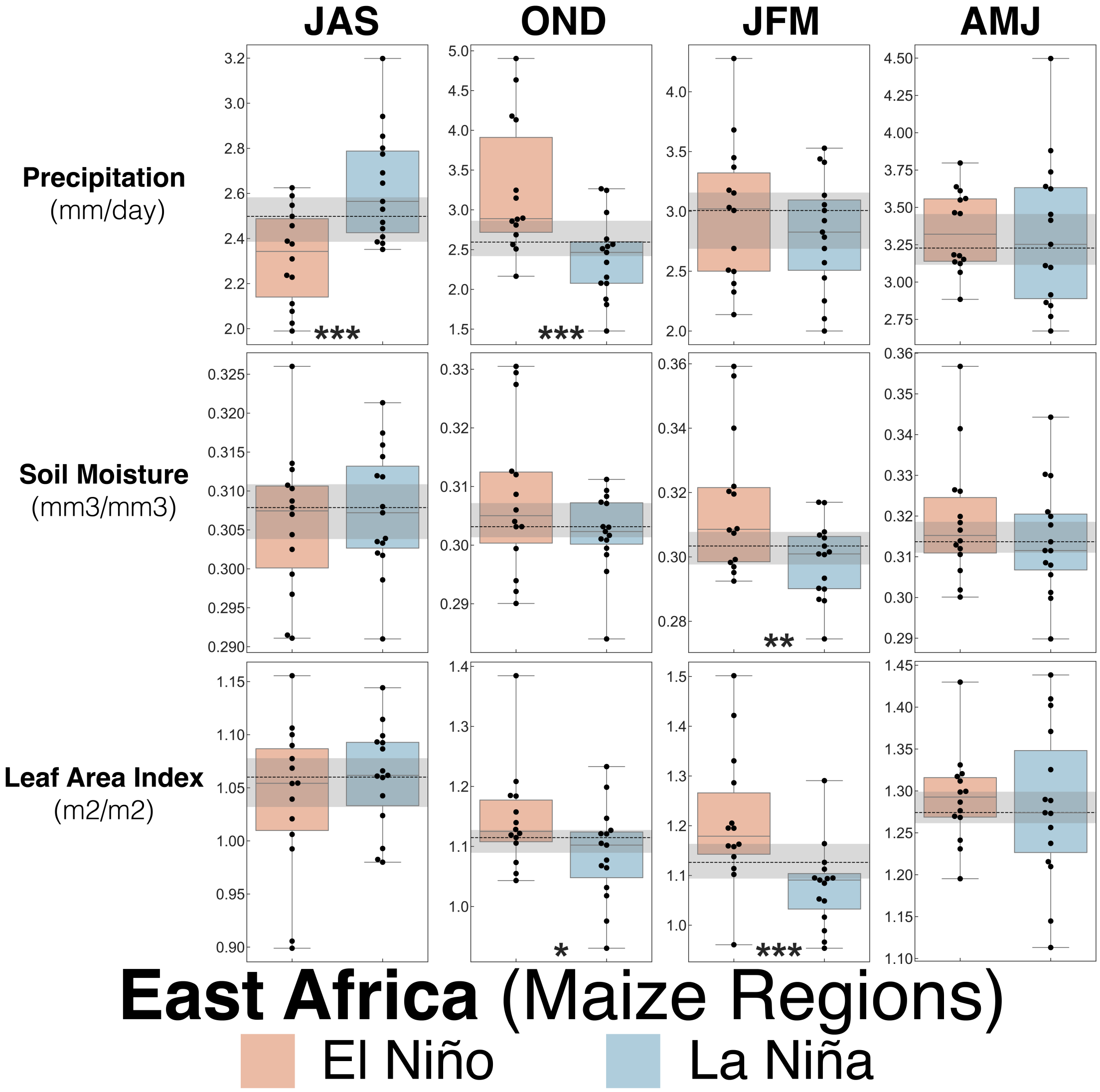

FIG. 7. Box and swarm plots of precipitation, soil moisture (200 cm), and LAI during El Niño and La Niña over East Africa. Each observation is the area-weighted average during the specified season over the maize cropping regions of East Africa identified in Figure 1. Grey shading indicates the central tercile of anomalies from all years in our datasets (1982–2020). As previously noted, July-August-September (JAS) and October-November-December (OND) anomalies are taken from the year corresponding with the peak in the ENSO event, while other seasons are from the following year. Asterisks indicate significance levels from a two-sample Wilcoxon rank sum test comparing El Niño and La Niña distributions: $*p \leq 0.10$, $**\,p \leq 0.05$, and $***p \leq 0.01$.

during El Niño, with the expected sign reversal and significantly drier conditions during La Niña in OND. These La Niña induced precipitation deficits are followed in JFM by significantly lower soil moisture and LAI.

Even in seasons with the strongest responses or largest differences between El Niño and La Niña, however, the spread across events can be substantial. For example, while median precipitation in maize regions of southern Africa is strongly and anomalously low during El Niño in JFM, only 8 of the 14 El Niño events themselves have anomalies that fall below the long-term central tercile (the grey shading). Indeed, 5 of the events (36%) had anomalies at or above the long-term median (dashed line). Similar results can be found for La Niña and precipitation deficits in OND in East Africa maize regions, where again the large spread means that 8 of the 15 La Niña events (53%) have precipitation anomalies that fall within or above the central tercile. This strongly suggests there may be some major limitations in the robustness of ENSO phases to predict major drought events within the maize growing areas of southern and East Africa, where crop production concerns are significant. We note that, in some cases, averaging of anomalies across maize regions may mask important spatial variability in the climate response to ENSO. In East Africa, for example, the negative aggregate JAS precipitation responses during El Niño (Figure 7) are primarily driven by the response over Ethiopia and Uganda, rather than Kenya and Tanzania (Figure 3).

Results are consistent using the alternative datasets, with some small, but possibly important, differences in LAI (Supplementary Figures 5–6). Over both southern and East Africa maize regions, absolute values of LAI from the GIMMS 4g dataset are overall higher than GLOBMAP and, in some cases, differences across ENSO phases are more significant. As an example, for southern Africa maize regions, GIMMS 4g has a significant LAI response during JFM (there is no significant difference in GLOBMAP during this season) and a more significant ($**p \leq 0.05$ in GLOBMAP vs $***p \leq 0.01$ in GIMMS 4g) response during AMJ. Despite these somewhat nuanced differences across datasets, however, the ultimate conclusions remain the same, regardless of which dataset is being considered.

d. ENSO Case Study Events in Maize Growing Regions

The high variance across ENSO events is further illustrated by examining the seasonal evolution of hydroclimate and vegetation across recent strong El Niño (1997/1998 and 2015/2016; $ONI > 2.0\,\mathrm{K}$) and La Niña (1998/1999 and 2010/2011; $ONI \leq -1.0\,\mathrm{K}$) events (Figure 8). Precipitation anomalies were substantially below the mean across nearly the entire wet season (October–February) during

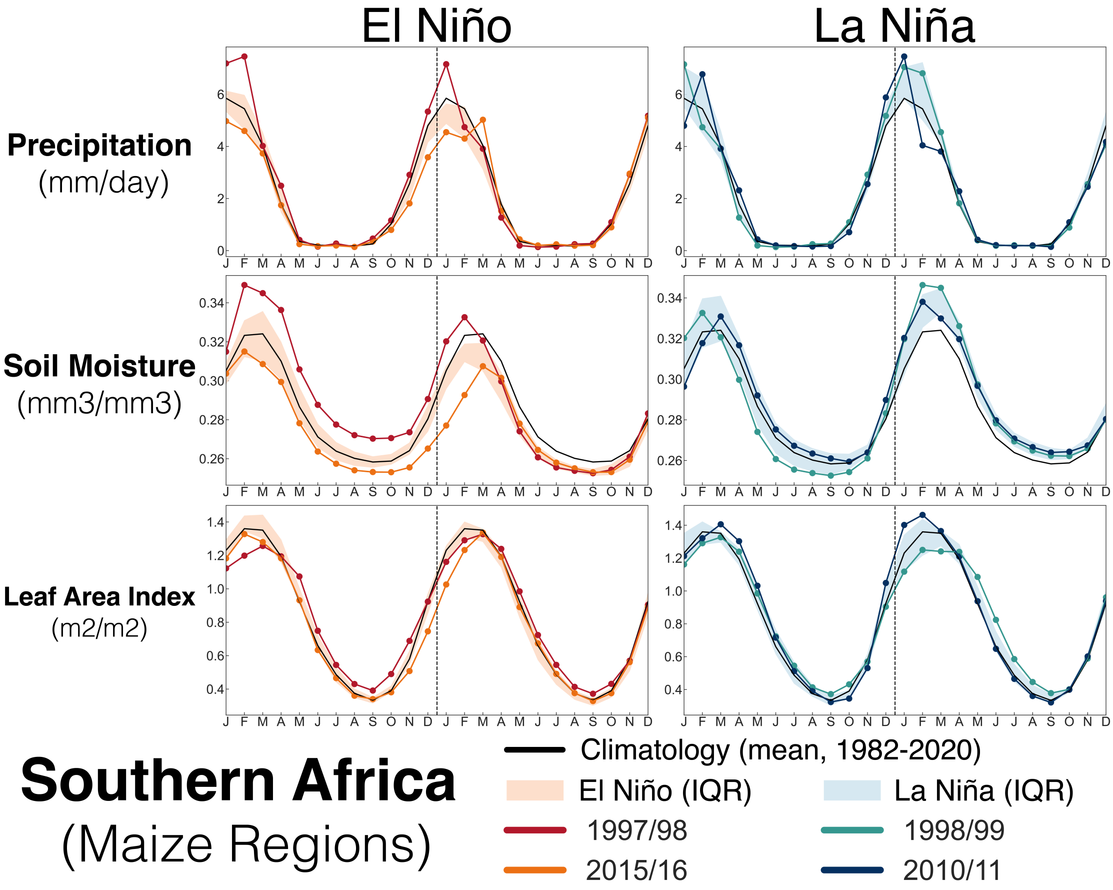

Fig. 8. Seasonal cycles of precipitation (mm/day), soil moisture (200 cm, mm3/mm3), and LAI (m2/m2), averaged over maize cropping regions of southern Africa. Mean climatology (1982–2020) is shown in the thin black line. The interquartile ranges for all El Niño and La Niña events are in the red and blue shading, respectively, and individual ENSO events are shown in the colored lines.

the 2015/2016 El Niño while 1997/1998 was above normal from September through January. Additionally, the 1997/1998 wet season began with soil moisture levels well above the mean. The wetter conditions in 1997/98 may explain why LAI was higher in most months during this event compared to 2015/2016. The 1998/1999 and 2010/2011 La Niña events both had above average precipitation during December and January, but 2010/2011 precipitation was higher and the wet season began with higher soil moisture levels. These overall wetter conditions may explain the higher early wet season LAI values, which drop substantially when precipitation drops below normal in February and March. By contrast, despite higher precipitation and soil moisture across most of the wet season, LAI is below normal from January through March in 1998/1999.

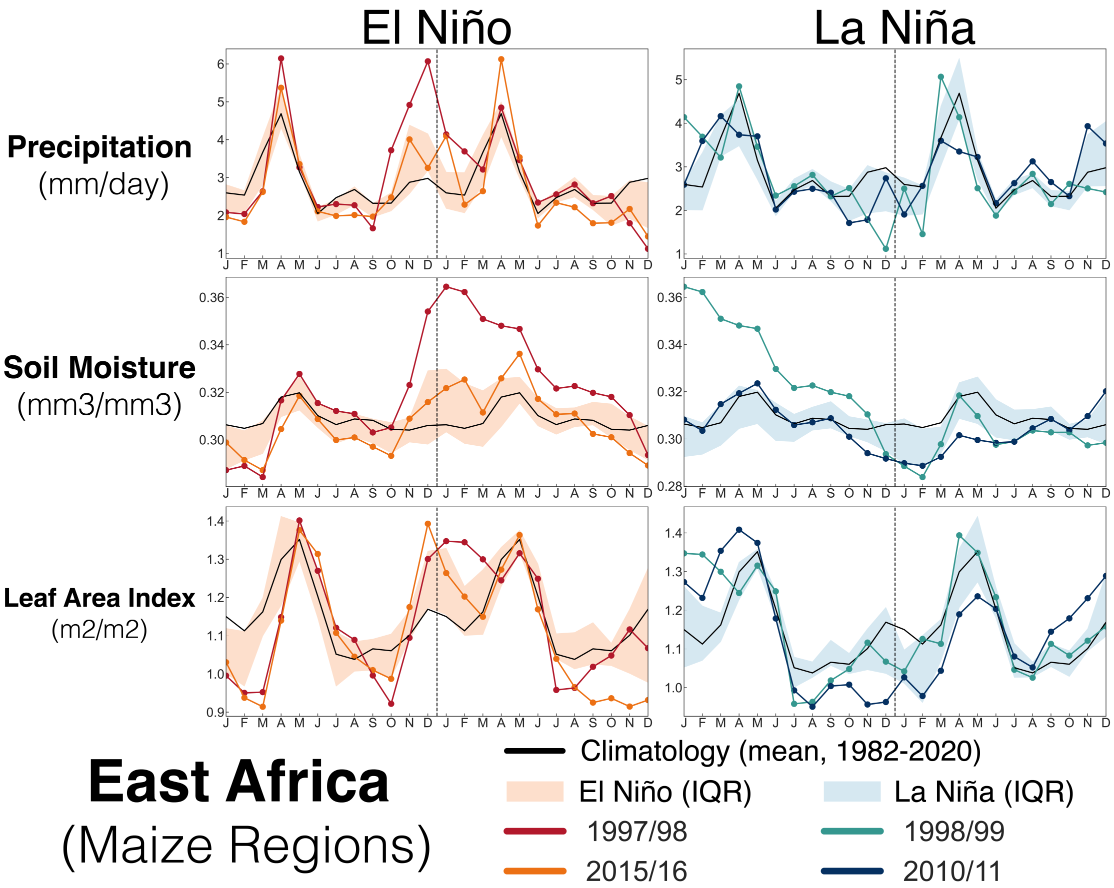

Fig. 9. Seasonal cycles of precipitation (mm/day), soil moisture (200 cm, mm3/mm3), and LAI (m2/m2), averaged over maize cropping regions of East Africa. Mean climatology (1982–2020) is shown in the thin black line. The interquartile ranges for all El Niño and La Niña events are in the red and blue shading, respectively, and individual ENSO events are shown in the colored lines.

Similar differences can be found across these ENSO events in East Africa (Figure 9). Consistent with expectations, both El Niño events have below normal precipitation during JAS and above normal precipitation in OND. However, the OND short rain precipitation surpluses are higher during 1997/1998 compared to 2015/2016, resulting in higher overall soil moisture levels that persisted across the following calendar year (1998). Precipitation was anomalously low for both La Niña events during October–February. However, initial soil moisture conditions in October were higher during 1998/1999, a consequence of the extremely high precipitation during the short rains from the El Niño in the previous year carrying forward, which may explain the overall higher LAI values compared to the 2010/2011 La Niña.

While there are some differences in anomaly magnitudes, the same analyses using the alternative datasets show similar results (Supplementary Figures 7-8). For example, GPCC precipitation over East Africa is also higher during the OND short rains in 1997/1998 compared to 2015/2016, and these high levels of precipitation are reflected in the anomalously high GLEAM root zone soil moisture that carried forward during the next calendar year.

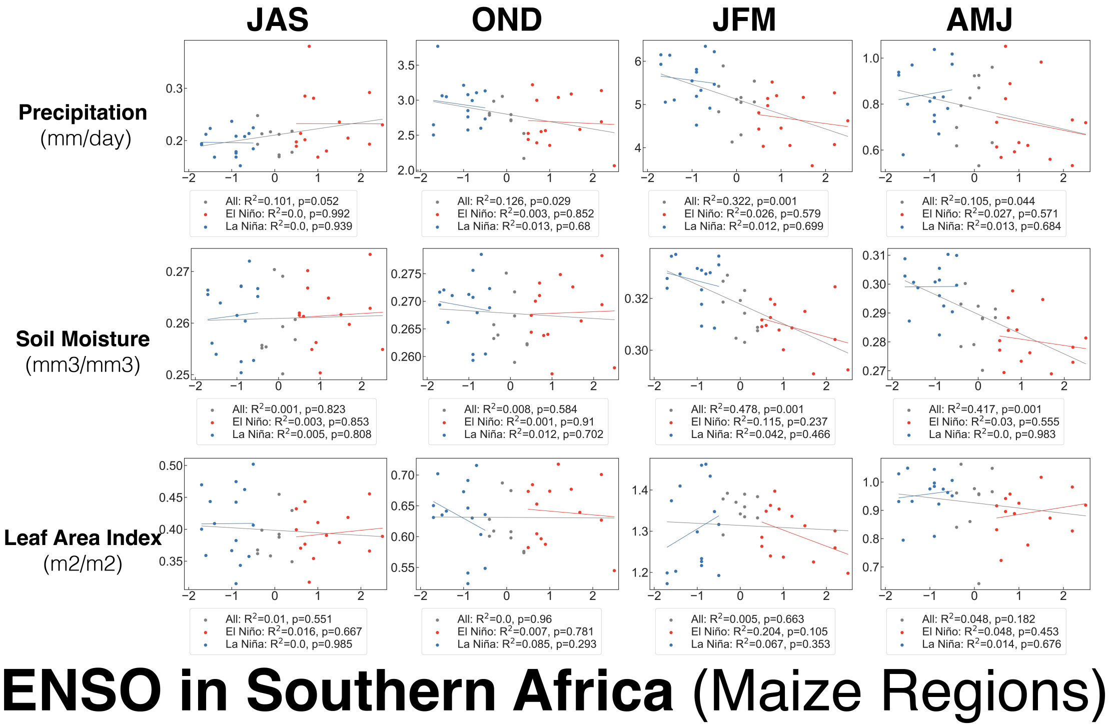

ENSO in Southern Africa (Maize Regions)

FIG. 10. Scatter plots and regressions between the DJF ONI index and precipitation (mm/day), soil moisture (200 cm, mm3/mm3), and LAI (m2/m2), averaged over maize cropping regions of southern Africa. Legends display R2 and significance levels for the regressions using all years (grey lines), El Niño years only (red lines), and La Niña years only (blue lines).

e. Teleconnection Strength and ENSO Event Magnitude

To investigate whether teleconnection strength scales with intensity of El Niño and La Niña events, we used linear regression analyses to compare our ENSO index (the DJF ONI) and climate and vegetation anomalies averaged over southern (Figures 10) and East Africa (Figures 11) maize regions. We conducted three different regressions: using all years (grey lines), El Niño events only (red lines), and La Niña events only (blue lines). Goodness of fit (R2) and significance levels (p-values) for the three different regressions in each season are shown in the legends.

Seasons with significant differences in the median between El Niño and La Niña events (Figures 6–7) also had significant regressions when using all years. For example, the regression with all years of JFM precipitation in southern Africa resolved over 30% of the underlying variance ($R^2 = 0.322$, $p \leq 0.001$). However, regressions using only El Niño or only La Niña years were weaker and largely insignificant, even for seasons where regressions using all years were skillful (e.g., JFM precipitation in southern Africa). We found nearly identical results when using the alternative datasets (Supplementary Figures 9 and 10). We therefore find no supporting evidence that event magnitude alone has an impact on teleconnection strength over these regions.

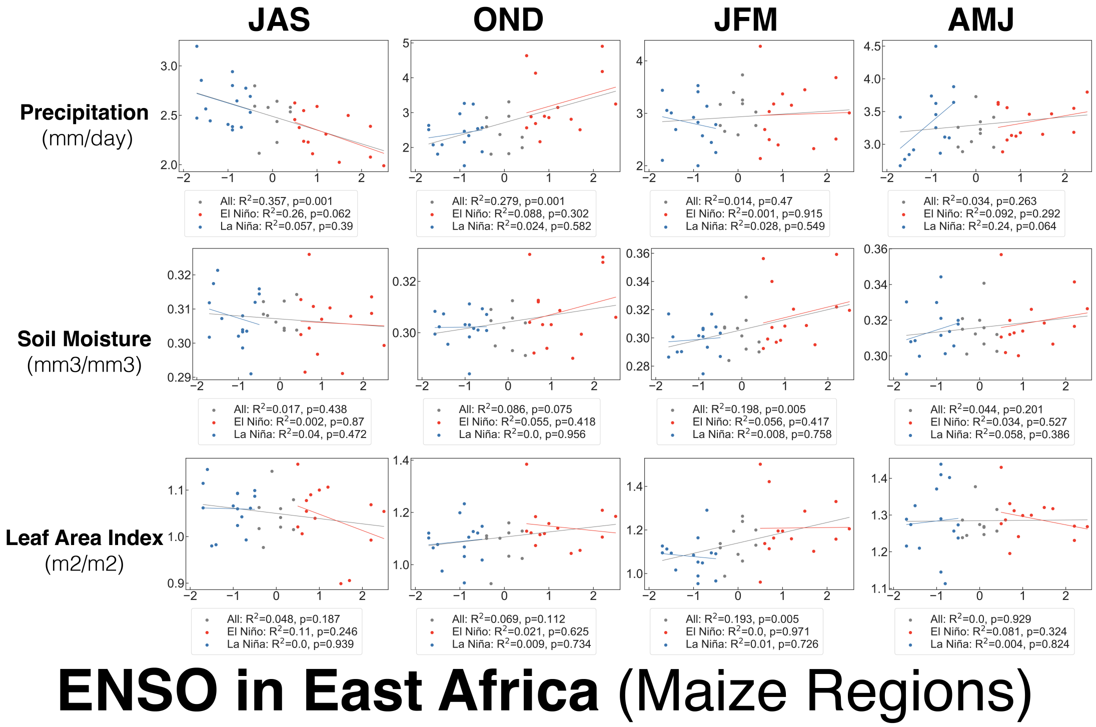

Fig. 11. Scatter plots and regressions between the DJF ONI index and precipitation (mm/day), soil moisture (200 cm, mm3/mm3), and LAI (m2/m2), averaged over maize cropping regions of East Africa. Legends display R2 and significance levels for the regressions using all years (grey lines), El Niño years only (red lines), and La Niña years only (blue lines).

f. Maize Yield Sensitivity to Hydroclimate

Maize yields in Kenya, Malawi, South Africa, and Zimbabwe have positive and significant ($p \leq 0.05$, black dots) correlations with hydroclimate averaged over the maize growing regions of these countries (Figure 12). Horizontal shading shows the planting (blue), growth (grey), and harvest (orange) periods associated with the maize growing seasons in each country. In Kenya, the two maize growing seasons coincide with the short (top shading) and long (bottom shading) rains, while in South Africa the two seasons are differentiated by region (top shading: west; bottom shading; east).

Over Kenya, yield and precipitation correlate significantly in April, the middle of the long rains maize planting season (March–May), followed by significant correlations in soil moisture and LAI that extend until the end of this growing season in September. The longer period of significant correlations with soil moisture and LAI, which is also seen in other countries, likely reflects the persistence of cumulative, antecedent precipitation anomalies embedded within these variables. In Malawi, correlations between yield and precipitation peak in January-February, near the beginning of the maize growing season, followed by significant soil moisture correlations during the latter part of the growing season in March and into the harvest period of April–June. Correlations with LAI are similarly higher during the May–June harvest period.

In South Africa, yield correlations with precipitation are significant in October in the year prior to harvest and in January-February of the harvest year. October is the main maize planting period in eastern South Africa, while December–January is the main planting period in the western part of the country, which may explain the dual peak. As with Kenya and Malawi, correlations with the other variables are lagged compared to precipitation, peaking in January–March for soil moisture and February–April for LAI. These months represent the latter part of the maize growing season in South Africa. Finally, correlations between yield and precipitation in Zimbabwe are strong and significant in February, roughly the middle of the maize growing season. This is followed by significant correlations in soil moisture and precipitation in the following months, continuing through and beyond the main harvest season of May–June. In several instances, crop yields correlate with soil moisture and LAI during months outside of the maize growing season: for example, LAI during October–November in Malawi. While these months are after the typical maize harvest, they do coincide with the planting period for maize, cotton, and peanuts the

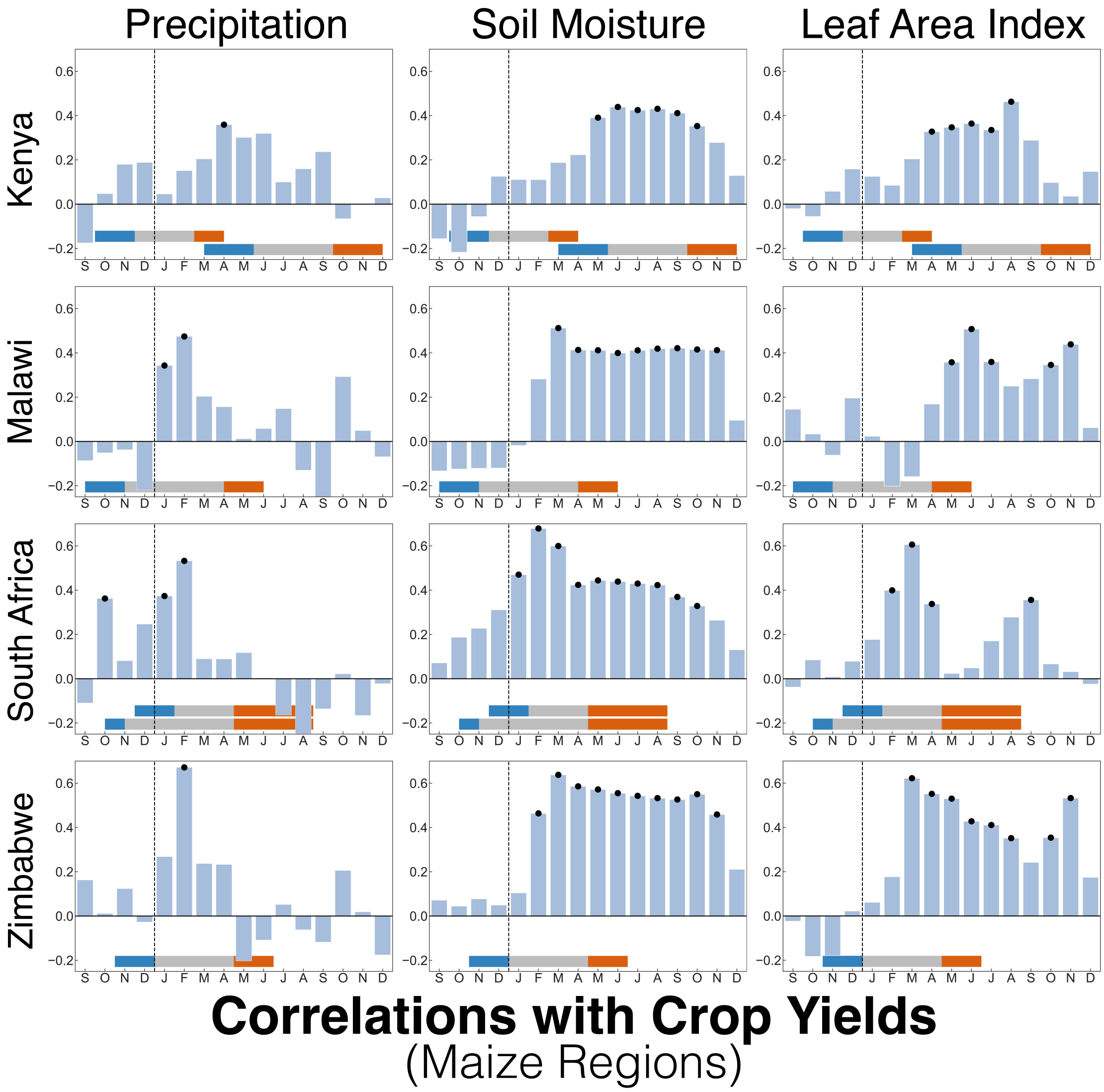

FIG. 12. Pearson's correlations between country-level maize crop yields and precipitation, soil moisture, and LAI averaged over maize cropping regions (Figure 1) within those countries (1983–2020). Correlations were calculated from July of the year prior to harvest (left side of dottted line) through October of the harvest year. Nominally significant correlations (n=38, $p \leq 0.05$) are indicated by the black dots. Horizontal shading indicates different phases of the maize growing season: planting (blue), growth (grey), and harvest (orange). Kenya and South Africa have two maize growing seasons. For Kenya, these correspond to the growing season associated with the short (top shading) and long (bottom shading) rains. For South Africa, these different seasons are associated with maize growing in the western (top shading) and eastern (bottom shading) maize regions.

following year. Given the strong persistence and lagged response of soil moisture and LAI to precipitation apparent in our previous analyses, this could reflect carry over of effects from one year or season to the next.

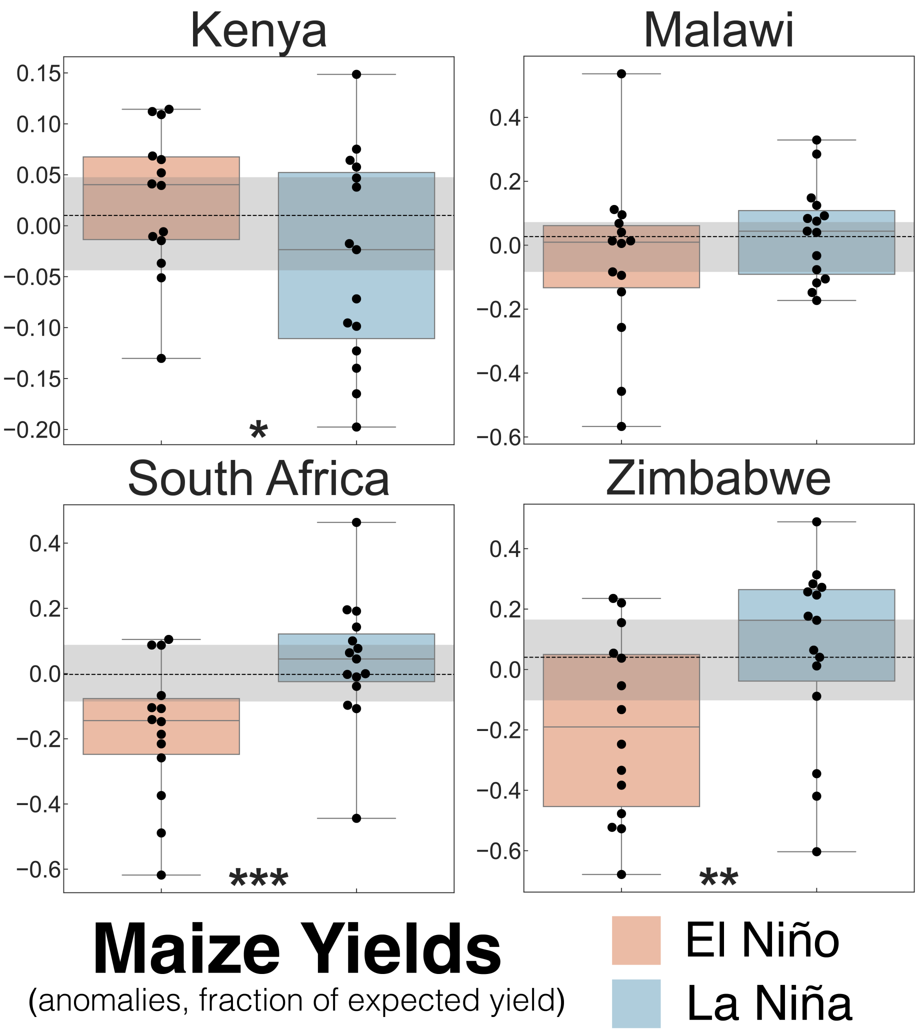

FIG. 13. Box and swarm plots of country-level maize crop yield anomalies during El Niño and La Niña events. Grey shading indicates the central tercile of anomalies from all years in the datasets (1983–2020). Yield anomalies are taken from the year following the peak of the ENSO event. Asterisks indicate significance levels from a two-sample Wilcoxon rank sum test comparing El Niño and La Niña distributions: $*p \leq 0.10$, $**p \leq 0.05$, and $***p \leq 0.01$.

g. Maize Yield Variability during ENSO Events

Consistent with broad expectations from the previous hydroclimate analyses, maize yields are typically below normal during La Niña events in Kenya and below normal during El Niño events in Malawi, South Africa, and Zimbabwe (Figure 13). Differences between median yield during La Niña versus El Niño events are only marginally significant for Kenya, with overall stronger differences in South Africa and Zimbabwe. Differences in yield between El Niño and La Niña events are not significant for Malawi, a result that may be at least partially attributable to its geographic location, sitting on the periphery of regions with the strongest ENSO teleconnections.

As with the hydroclimate analyses of maize growing areas in these regions, there is a large spread across ENSO events in maize yield anomalies. The most consistent responses are during El Niño in South Africa (10 of 14 events below the central tercile; 71%) and Zimbabwe (8 of 14 events; 57%). In Kenya and Malawi, less than half of the events have yield anomalies that fall in the lower tercile during the drier ENSO phases. For Kenya, and to some extent South Africa and Zimbabwe, however, the large variability in yield across events is consistent with the high variability in hydroclimate impacts across ENSO events in these regions.

4. Discussion and Conclusions

Our results highlight the complexity of ENSO teleconnections to hydroclimate, vegetation, and agriculture across southern and East Africa. For precipitation, these results are similar to decision making aids like the "IRI cartoon" (Lenssen et al. 2020) and FEWS NET fact sheets (FEWS NET 2020), though the methods of arriving at these maps differ in terms of time periods considered and thresholds for wet and dry. Our analysis goes beyond these efforts to quantify the stability of these teleconnection patterns for precipitation and other variables closely connected to agricultural and food security outcomes (soil moisture, LAI, crop yields). We find stronger and more stable associations (i.e., high anomaly sign consensus) between regional hydroclimate, vegetation, and crop yield responses and the drought associated ENSO events: El Niño in southern Africa and La Niña in East Africa. South Africa, for example, has stronger and more consistent sign maize yield anomalies (negative) and better separation from the central tercile during El Niño (drought), compared to La Niña (wetter than normal). Teleconnection strength appears largely insensitive to the intensity of the El Niño and La Niña events themselves over maize growing areas.

Further, even in cases where ENSO teleconnections are strong, there is high variability in the magnitude and sign of anomalies across events and ENSO phases within maize growing regions. For example, despite the ostensible importance of La Niña for East Africa drought, fewer than half of these events are associated with lower tercile OND short rain precipitation in maize growing areas of this region (Figure 7). This high variability across events also extends to maize yields (Figure 13), especially in Kenya and Malawi where drought related ENSO phases caused lower tercile maize yield anomalies in less than half of all events. There is consequently a substantial amount of residual variability in both hydroclimate and crop yields independent from ENSO, highlighting the challenges related to seasonal prediction, especially at finer, subregional spatial scales. Ultimately, while ENSO does offer some significant power for predicting conditions related to food insecurity over southern and East Africa, there are major limitations in relying on this mode as the sole or primary source of skill for seasonal forecasts.

Our analyses and conclusions may be sensitive to several limitations in our study design and methods. The short period of study (39 years) limits the number of ENSO events that can be sampled: 14 for El Niño and 15 for La Niña. This is a constraint of the datasets we analyzed and the lack of longer term high quality alternatives, especially for the remotely sensed LAI and maize yield data. While this represents a substantial increase in events analyzed compared to previous similar studies (e.g., Sazib et al. 2020), we are still likely undersampling important variability in the ENSO system. For example, decadal scale variability in ENSO and tropical Pacific SSTs is well established (Newman et al. 2016) and known to affect teleconnection strength (Gershunov and Barnett 1998; Power et al. 2006). Additionally, other climate modes, forcings, and even just internal atmospheric variability influence how strongly canonical ENSO teleconnections are realized (Hoell et al. 2014, 2015, 2017; Taschetto et al. 2020).

We also recognize that our relatively simple approach for defining El Niño and La Niña will mask some important sources of diversity across ENSO events. For example, both the seasonal evolution (Vimont et al. 2022) and geographic center of action (Kao and Yu 2009) for the critical SST anomalies can vary substantially across ENSO events. Such details can affect teleconnection strength between ENSO and regional climate (Paek et al. 2017), but are unlikely to be captured in our relative simple definition which uses fixed seasonal and geographic windows for the SST anomalies. Given the short length of our dataset and limited sampling of events, we are reluctant to draw any strong conclusions about ENSO event diversity and teleconnection strength beyond our analyses of event intensity, though we believe our approach to event definition is appropriate for our study goals.

Our results suggest that ENSO teleconnection strength in southern and East Africa does not scale with ENSO event magnitude, a finding at odds with other studies (e.g., Pomposi et al. 2018). Such differences between our study and others could arise for several reasons. First, our analyses of ENSO event magnitude focused specifically on the maize growing areas of southern and East Africa, rather than the larger regions. Our results therefore likely reflect some degree of spatial variability in ENSO teleconnection strength, something apparent from the anomaly sign consensus analysis (Figures 3 and 4). Second, our results may be affected by undersampling of ENSO variability. Other studies have circumvented this limitation using climate model experiments (e.g., Pomposi et al. 2018), a potentially useful approach but one that depends on how well the models simulate ENSO dynamics and teleconnections.

The data on maize cropping areas and yields also have some significant uncertainties. For crop areas, we chose a 1% area fraction for our cropping area masks used in the area averaged hydroclimate comparisons. As noted previously, this choice represented a trade off between a higher cropping density threshold that would severely restrict the number of grid cells versus including all regions with any documented cropping, regardless of how important these areas are for national production (Supplementary Figure 1). The quality of the crop yield data also varies across different countries. Yields from South Africa, for example, are likely the most accurate among the countries we analyzed because they are the largest maize producer in the region and a significant exporter to other countries. More food insecure countries (e.g., Zimbabwe), however, often have lower quality data. Additionally, while we standardized and detrended the yield data to isolate yield variability due to climate, this is an imperfect approach and also likely does not address the full suite of management changes that could affect relationships between yield and climate. While our analysis focuses on the abiotic pathways by which ENSO affects crop yields, indirect biotic pathways are likely also present. The relative incidence of disease and pests, such as locusts, depends in part on the crop growing season climate, which is affected by ENSO. Our analyses estimating the influence of ENSO on crop yields, therefore, should be interpreted as including both the direct impact of abiotic stress on crop yields and the indirect influence of abiotic growing conditions on the incidence of biotic stresses. Separating out the relative importance of the biotic and abiotic pathways during ENSO years, however, requires further research.

Even with these limitations, we believe our study offers strong motivation to explore the potential predictive value of other modes of variability in the climate system and the role of initial conditions. The importance of initial conditions is highlighted in the case study analysis, most notably in the persistence of extreme high soil moisture anomalies in East Africa maize regions during the transition from the 1997/98 El Niño to the 1998/99 La Niña (Figure 9). This suggests that a product that combines initial conditions, specifically soil moisture and vegetation, with ENSO-informed precipitation forecasts may provide useful information to users. Currently FLDAS-Forecast (Hazra et al. 2023), NASA's hydrologic forecast system for food insecurity based on the North American Multi-Model Ensemble (NMME) forecasts, does provide this information for Africa. But this work could be further developed, especially if initial conditions other than soil moisture (e.g., LAI) were incorporated into the modeling framework.

Alternative modes of climate variability should also be explored and investigated, including how they may interfere with expected ENSO teleconnections and whether they may offer additional sources of skill for seasonal forecasts. One particularly important pattern is the Indian Ocean Dipole (IOD), a subtropical mode of ocean-atmosphere variability in the Indian Ocean that can be triggered by ENSO events or evolve independently (Saji et al. 1999; Webster et al. 1999). Peaking during boreal autumn (SON) (Feba et al. 2021), positive phases of the IOD are associated with wetter conditions in East Africa and drier conditions over southern Africa (Saji and Yamagata 2003; Scanlon et al. 2022). Depending on the phasing with ENSO, IOD events therefore have strong potential to amplify or counteract ENSO forced precipitation anomalies (Saji and Yamagata 2003). Another pattern originating in the Indian Ocean, the Southern Indian Ocean Dipole (SIOD) (Hoell et al. 2017), is also important over southern Africa. The SIOD peaks in February and, when in phase with ENSO (e.g., +SIOD and El Niño), weakens the ENSO teleconnection. Incorporating information from these modes may, therefore, improve the fidelity of seasonal forecasts over southern and East Africa. However, unlike ENSO, the time horizon of skill for these modes is more limited. Skillful prediction of the IOD, for example, is limited to 6 months, with the strongest skill at 4 months, though analyses of decadal prediction model experiments suggest skill may extend to 17 months (Feba et al. 2021). Regardless, if skillful forecasts of these and other modes can be improved, then they may provide improved constraints for ENSO-informed seasonal climate and food forecasts within Sub-Saharan Africa.

Acknowledgments. This publication was made possible through the support of the Bureau of Humanitarian Assistance, U.S. Agency for International Development, under the terms of PAPA #AID-720BHAH00005 ”Famine Early Warning Systems Network (FEWS NET)”. The opinions expressed in this presentation are those of the authors and do not necessarily reflect the views of the U.S. Agency for International Development of the United States government. FLDAS simulations were made possible by support from the NASA Center for Climate Simulation (NCCS). SS supported by U.S. Geological Survey, United States Grant #G21AC00026. Support also provided by the NASA Harvest Consortium (NASA Applied Sciences grant # 80NSSC17K0625).

Data availability statement. FLDAS soil moisture and precipitation: `https://ldas.gsfc.nasa.gov/fldas/fldas-data-download`. GLOBMAP leaf area index: `https://zenodo.org/record/4700264#.ZEKk_XbMI23`. GEOGLAM cropping areas `https://zenodo.org/record/7230863#.ZFpdEnbMI21`. FAOSTAT Maize yields: `https://data.apps.fao.org/catalog/dataset/crop-production-yield-harvested-area-global-national-annual-faostat`. GPCC Precipitation: `https://opendata.dwd.de/climate_environment/GPCC/html/fulldata-monthly_v2022_doi_download.html`. GLEAM Soil Moisture: `https://www.gleam.eu/`. GIMMS 4g LAI: `https://zenodo.org/record/7649108`.

References

Anderson, W., and Coauthors, 2023: Climate variability and simultaneous breadbasket yield shocks as observed in long-term yield records. *Agricultural and Forest Meteorology*, **331**, 109 321, https://doi.org/https://doi.org/10.1016/j.agrformet.2023.109321, URL https://www.sciencedirect.com/science/article/pii/S0168192323000151.

Anderson, W. B., R. Seager, W. Baethgen, M. Cane, and L. You, 2019: Synchronous crop failures and climate-forced production variability. *Science Advances*, **5 (7)**, eaaw1976, https://doi.org/10.1126/sciadv.aaw1976, URL https://www.science.org/doi/abs/10.1126/sciadv.aaw1976, https://www.science.org/doi/pdf/10.1126/sciadv.aaw1976.

Anttila-Hughes, J. K., A. S. Jina, and G. C. McCord, 2021: ENSO impacts child undernutrition in the global tropics. *Nature Communications*, **12 (1)**, 5785, https://doi.org/

10.1038/s41467-021-26048-7, URL https://doi.org/10.1038/s41467-021-26048-7.

Anyamba, A., E. Glennie, and J. Small, 2018: Teleconnections and Interannual Transitions as Observed in African Vegetation: 2015–2017. *Remote Sensing*, **10 (7)**, https://doi.org/10.3390/rs10071038.

Anyamba, A., C. J. Tucker, and R. Mahoney, 2002: From El Niño to La Niña: Vegetation Response Patterns over East and Southern Africa during the 1997–2000 Period. *Journal of Climate*, **15 (21)**, 3096–3103, https://doi.org/https://doi.org/10.1175/1520-0442(2002)015<3096:FENOTL>2.0.CO;2, URL https://journals.ametsoc.org/view/journals/clim/15/21/1520-0442_2002_015_3096_fenotl_2.0.co_2.xml.

Ashcroft, L., J. Gergis, and D. J. Karoly, 2016: Long-term stationarity of El Niño–Southern Oscillation teleconnections in southeastern Australia. *Climate Dynamics*, **46 (9)**, 2991–3006, https://doi.org/10.1007/s00382-015-2746-3.

Backer, D., and T. Billing, 2021: Validating Famine Early Warning Systems Network projections of food security in Africa, 2009–2020. *Global Food Security*, **29**, 100 510, https://doi.org/https://doi.org/10.1016/j.gfs.2021.100510, URL https://www.sciencedirect.com/science/article/pii/S2211912421000201.

Barnston, A. G., M. K. Tippett, M. Ranganathan, and M. L. L'Heureux, 2019: Deterministic skill of ENSO predictions from the North American Multimodel Ensemble. *Climate Dynamics*, **53 (12)**, 7215–7234, https://doi.org/10.1007/s00382-017-3603-3, URL https://doi.org/10.1007/s00382-017-3603-3.

Becker-Reshef, I., B. Barker, A. Whitcraft, P. Oliva, K. Mobley, C. Justice, and R. Sahajpal, 2023: Crop Type Maps for Operational Global Agricultural Monitoring. *Scientific Data*, **10 (1)**, 172, https://doi.org/10.1038/s41597-023-02047-9, URL https://doi.org/10.1038/s41597-023-02047-9.

Bosilovich, M. G., S. Akella, L. Coy, and R. e. a. Cullather, 2015: MERRA-2: Initial Evaluation of the Climate. Tech. rep., NASA Goddard Space Flight Center.

Cai, W., and Coauthors, 2020: Climate impacts of the El Niño–Southern Oscillation on South America. *Nature Reviews Earth & Environment*, **1 (4)**, 215–231, https://doi.org/10.1038/s43017-020-0040-3, URL https://doi.org/10.1038/s43017-020-0040-3.

Calderini, D. F., and G. A. Slafer, 1998: Changes in yield and yield stability in wheat during the 20th century. *Field Crops Research*, **57 (3)**, 335–347, https://doi.org/https://doi.org/10.1016/S0378-4290(98)00080-X, URL https://www.sciencedirect.com/science/article/pii/S037842909800080X.

Cao, S., and Coauthors, 2023: Spatiotemporally consistent global dataset of the GIMMS Leaf Area Index (GIMMS LAI4g) from 1982 to 2020. *Earth System Science Data Discussions*, **15**, 4877–4899, https://doi.org/https://doi.org/10.5194/essd-15-4877-202, URL https://essd.copernicus.org/preprints/essd-2023-68/.

Choularton, R. J., and P. K. Krishnamurthy, 2019: How accurate is food security early warning? Evaluation of FEWS NET accuracy in Ethiopia. *Food Security*, **11 (2)**, 333–344, https://doi.org/10.1007/s12571-019-00909-y, URL https://doi.org/10.1007/s12571-019-00909-y.

Derber, J. C., D. F. Parrish, and S. J. Lord, 1991: The New Global Operational Analysis System at the National Meteorological Center. *Weather and Forecasting*, **6 (4)**, 538–547, https://doi.org/https://doi.org/10.1175/1520-0434(1991)006<0538:TNGOAS>2.0.CO;2, URL https://journals.ametsoc.org/view/journals/wefo/6/4/1520-0434_1991_006_0538_tngoas_2_0_co_2.xml.

Deser, C., I. R. Simpson, K. A. McKinnon, and A. S. Phillips, 2017: The Northern Hemisphere Extratropical Atmospheric Circulation Response to ENSO: How Well Do We Know It and How Do We Evaluate Models Accordingly? *Journal of Climate*, **30 (13)**, 5059–5082, https://doi.org/https://doi.org/10.1175/JCLI-D-16-0844.1, URL https://journals.ametsoc.org/view/journals/clim/30/13/jcli-d-16-0844.1.xml.

Dirmeyer, P. A., Y. Jin, B. Singh, and X. Yan, 2013: Evolving Land–Atmosphere Interactions over North America from CMIP5 Simulations. *Journal of Climate*, **26 (19)**, 7313–7327, https://doi.org/10.1175/JCLI-D-12-00454.1.

Dorigo, W., and Coauthors, 2017: ESA CCI Soil Moisture for improved Earth system understanding: State-of-the art and future directions. *Remote Sensing of Environment*, **203**, 185–215, https://doi.org/https://doi.org/10.1016/j.rse.2017.07.001, URL https://www.sciencedirect.com/science/article/pii/S0034425717303061.

Feba, F., K. Ashok, M. Collins, and S. R. Shetye, 2021: Emerging Skill in Multi-Year Prediction of the Indian Ocean Dipole. *Frontiers in Climate*, **3**, https://doi.org/10.3389/fclim.2021.736759, URL https://www.frontiersin.org/articles/10.3389/fclim.2021.736759.

FEWS NET, 2020: El Niño and Precipitation. *Agroclimatology Fact Sheet Series*, **1**, 1–2.

Food and Agriculture Organization of the United Nations, 2023: FAOSTAT Statistical Database, CC BY-NC-SA 3.0 IGO. Tech. rep., United Nations. URL https://www.fao.org/faostat/en/.

Funk, C., and Coauthors, 2015: The climate hazards infrared precipitation with stations—a new environmental record for monitoring extremes. *Scientific Data*, **2 (1)**, 150 066, https://doi.org/10.1038/sdata.2015.66, URL https://doi.org/10.1038/sdata.2015.66.

Funk, C., and Coauthors, 2019: Recognizing the Famine Early Warning Systems Network: Over 30 Years of Drought Early Warning Science Advances and Partnerships Promoting Global Food Security. *Bulletin of the American Meteorological Society*, **100 (6)**, 1011–1027, https://doi.org/10.1175/BAMS-D-17-0233.1, URL https://journals.ametsoc.org/view/journals/bams/100/6/bams-d-17-0233.1.xml.

Gershunov, A., and T. P. Barnett, 1998: Interdecadal Modulation of ENSO Teleconnections. *Bulletin of the American Meteorological Society*, **79 (12)**, 2715–2725, https://doi.org/10.1175/1520-0477(1998)079<2715:IMOET>2.0.CO;2.

Giannini, A., R. Saravanan, and P. Chang, 2004: The preconditioning role of Tropical Atlantic Variability in the development of the ENSO teleconnection: implications for the prediction of Nordeste rainfall. *Climate Dynamics*, **22 (8)**, 839–855, https://doi.org/10.1007/s00382-004-0420-2, URL https://doi.org/10.1007/s00382-004-0420-2.

Goddard, L., and M. Dilley, 2005: El Niño: Catastrophe or Opportunity. *Journal of Climate*, **18 (5)**, 651–665, https://doi.org/https://doi.org/10.1175/JCLI-3277.1, URL https://journals.ametsoc.org/view/journals/clim/18/5/jcli-3277.1.xml.

Goddard, L., S. J. Mason, S. E. Zebiak, C. F. Ropelewski, R. Basher, and M. A. Cane, 2001: Current approaches to seasonal to interannual climate predictions. *International Journal of*

Climatology, **21 (9)**, 1111–1152, https://doi.org/https://doi.org/10.1002/joc.636, URL https://doi.org/10.1002/joc.636.

Gruber, A., W. A. Dorigo, W. Crow, and W. Wagner, 2017: Triple Collocation-Based Merging of Satellite Soil Moisture Retrievals. *IEEE Transactions on Geoscience and Remote Sensing*, **55 (12)**, 6780–6792, https://doi.org/10.1109/TGRS.2017.2734070.

Guimarães Nobre, G., S. Muis, T. I. E. Veldkamp, and P. J. Ward, 2019: Achieving the reduction of disaster risk by better predicting impacts of el niño and la niña. *Progress in Disaster Science*, **2**, 100 022, https://doi.org/https://doi.org/10.1016/j.pdisas.2019.100022, URL https://www.sciencedirect.com/science/article/pii/S2590061719300225.

Hazra, A., and Coauthors, 2023: NASA's NMME-based S2S hydrologic forecast system for food insecurity early warning in southern Africa. *Journal of Hydrology*, **617**, 129 005, https://doi.org/https://doi.org/10.1016/j.jhydrol.2022.129005, URL https://www.sciencedirect.com/science/article/pii/S002216942201575X.

Hoell, A., M. Barlow, M. C. Wheeler, and C. Funk, 2014: Disruptions of El Niño–Southern Oscillation Teleconnections by the Madden–Julian Oscillation. *Geophysical Research Letters*, **41 (3)**, 998–1004, https://doi.org/https://doi.org/10.1002/2013GL058648, URL https://doi.org/10.1002/2013GL058648.

Hoell, A., C. Funk, T. Magadzire, J. Zinke, and G. Husak, 2015: El Niño–Southern Oscillation diversity and Southern Africa teleconnections during Austral Summer. *Climate Dynamics*, **45 (5)**, 1583–1599, https://doi.org/10.1007/s00382-014-2414-z, URL https://doi.org/10.1007/s00382-014-2414-z.

Hoell, A., C. Funk, J. Zinke, and L. Harrison, 2017: Modulation of the Southern Africa precipitation response to the El Niño Southern Oscillation by the subtropical Indian Ocean Dipole. *Climate Dynamics*, **48 (7)**, 2529–2540, https://doi.org/10.1007/s00382-016-3220-6, URL https://doi.org/10.1007/s00382-016-3220-6.

Iizumi, T., J.-J. Luo, A. J. Challinor, G. Sakurai, M. Yokozawa, H. Sakuma, M. E. Brown, and T. Yamagata, 2014: Impacts of El Niño Southern Oscillation on the global yields of major crops. *Nature Communications*, **5 (1)**, 3712, https://doi.org/10.1038/ncomms4712, URL https://doi.org/10.1038/ncomms4712.

Jong, B.-T., M. Ting, R. Seager, N. Henderson, and D. E. Lee, 2018: Role of Equatorial Pacific SST Forecast Error in the Late Winter California Precipitation Forecast for the 2015/16 El Niño. *Journal of Climate*, **31 (2)**, 839–852, https://doi.org/10.1175/JCLI-D-17-0145.1, URL https://journals.ametsoc.org/view/journals/clim/31/2/jcli-d-17-0145.1.xml.

Jung, H. C., A. Getirana, K. R. Arsenault, S. Kumar, and I. Maigary, 2019: Improving surface soil moisture estimates in West Africa through GRACE data assimilation. *Journal of Hydrology*, **575**, 192–201, https://doi.org/https://doi.org/10.1016/j.jhydrol.2019.05.042, URL https://www.sciencedirect.com/science/article/pii/S0022169419304871.

Kao, H.-Y., and J.-Y. Yu, 2009: Contrasting Eastern-Pacific and Central-Pacific Types of ENSO. *Journal of Climate*, **22 (3)**, 615 – 632, https://doi.org/https://doi.org/10.1175/2008JCLI2309.1, URL https://journals.ametsoc.org/view/journals/clim/22/3/2008jcli2309.1.xml.

Kiflie, K. A., and L. Tao, 2020: Opposite Effects of ENSO on the Rainfall over the Northern and Equatorial Great Horn of Africa and Possible Causes. *Advances in Meteorology*, **2020**, 9028 523, https://doi.org/10.1155/2020/9028523, URL https://doi.org/10.1155/2020/9028523.

Kogan, F., and W. Guo, 2017: Strong 2015–2016 El Niño and implication to global ecosystems from space data. *International Journal of Remote Sensing*, **38 (1)**, 161–178, https://doi.org/10.1080/01431161.2016.1259679, URL https://doi.org/10.1080/01431161.2016.1259679.

Korecha, D., and A. G. Barnston, 2007: Predictability of June–September Rainfall in Ethiopia. *Monthly Weather Review*, **135 (2)**, 628–650, https://doi.org/https://doi.org/10.1175/MWR3304.1, URL https://journals.ametsoc.org/view/journals/mwre/135/2/mwr3304.1.xml.

Krishnamurthy, P. K., R. J. Choularton, and P. Kareiva, 2020: Dealing with uncertainty in famine predictions: How complex events affect food security early warning skill in the Greater Horn of Africa. *Global Food Security*, **26**, 100 374, https://doi.org/https://doi.org/10.1016/j.gfs.2020.100374, URL https://www.sciencedirect.com/science/article/pii/S2211912420300274.

Kumar, K. K., B. Rajagopalan, M. Hoerling, G. Bates, and M. Cane, 2006: Unraveling the Mystery of Indian Monsoon Failure During El Niño. *Science*, **314 (5796)**, 115–119, https://doi.org/10.1126/science.1131152, URL https://doi.org/10.1126/science.1131152.

Lenssen, N. J. L., L. Goddard, and S. Mason, 2020: Seasonal forecast skill of enso teleconnection maps. *Weather and Forecasting*, **35 (6)**, 2387–2406, https://doi.org/10.1175/WAF-D-19-0235.1, URL https://journals.ametsoc.org/view/journals/wefo/35/6/WAF-D-19-0235.1.xml.

Liu, Y., R. Liu, and J. M. Chen, 2012: Retrospective retrieval of long-term consistent global leaf area index (1981–2011) from combined AVHRR and MODIS data. *Journal of Geophysical Research: Biogeosciences*, **117 (G4)**, https://doi.org/https://doi.org/10.1029/2012JG002084, URL https://doi.org/10.1029/2012JG002084.

Lobell, D. B., and C. B. Field, 2007: Global scale climate–crop yield relationships and the impacts of recent warming. *Environmental Research Letters*, **2 (1)**, 014 002, https://doi.org/10.1088/1748-9326/2/1/014002, URL https://dx.doi.org/10.1088/1748-9326/2/1/014002.

Lobell, D. B., and C. Tebaldi, 2014: Getting caught with our plants down: the risks of a global crop yield slowdown from climate trends in the next two decades. *Environmental Research Letters*, **9 (7)**, 074 003, https://doi.org/10.1088/1748-9326/9/7/074003, URL https://dx.doi.org/10.1088/1748-9326/9/7/074003.

Martens, B., and Coauthors, 2017: GLEAM v3: satellite-based land evaporation and root-zone soil moisture. *Geoscientific Model Development*, **10 (5)**, 1903–1925, https://doi.org/10.5194/gmd-10-1903-2017, URL https://www.geosci-model-dev.net/10/1903/2017/.

McNally, A., S. Shukla, K. R. Arsenault, S. Wang, C. D. Peters-Lidard, and J. P. Verdin, 2016: Evaluating ESA CCI soil moisture in East Africa. *International Journal of Applied Earth Observation and Geoinformation*, **48**, 96–109, https://doi.org/https://doi.org/10.1016/j.jag.2016.01.001, URL https://www.sciencedirect.com/science/article/pii/S0303243416300010, advances in the Validation and Application of Remotely Sensed Soil Moisture - Part 2.

McNally, A., and Coauthors, 2017: A land data assimilation system for sub-Saharan Africa food and water security applications. *Scientific Data*, **4 (1)**, 170 012, https://doi.org/10.1038/sdata.2017.12, URL https://doi.org/10.1038/sdata.2017.12.

Miralles, D. G., T. R. H. Holmes, R. A. M. De Jeu, J. H. Gash, A. G. C. A. Meesters, and A. J. Dolman, 2011: Global land-surface evaporation estimated from satellite-based observations. *Hydrology and Earth System Sciences*, **15 (2)**, 453–469, https://doi.org/10.5194/hess-15-453-2011, URL https://hess.copernicus.org/articles/15/453/2011/.

Newman, M., and Coauthors, 2016: The Pacific Decadal Oscillation, Revisited. *Journal of Climate*, **29 (12)**, 4399–4427, https://doi.org/https://doi.org/10.1175/JCLI-D-15-0508.1, URL https://journals.ametsoc.org/view/journals/clim/29/12/jcli-d-15-0508.1.xml.

Nicholson, S. E., 2017: Climate and climatic variability of rainfall over eastern Africa. *Reviews of Geophysics*, **55 (3)**, 590–635, https://doi.org/10.1002/2016RG000544.

Nicholson, S. E., and J. Kim, 1997: THE RELATIONSHIP OF THE EL NIÑO–SOUTHERN OSCILLATION TO AFRICAN RAINFALL. *International Journal of Climatology*, **17 (2)**, 117–135, https://doi.org/https://doi.org/10.1002/(SICI)1097-0088(199702)17:2<117::AID-JOC84>3.0.CO;2-O, URL https://doi.org/10.1002/(SICI)1097-0088(199702)17:2<117::AID-JOC84>3.0.CO;2-O.

Paek, H., J.-Y. Yu, and C. Qian, 2017: Why were the 2015/2016 and 1997/1998 extreme El Niños different? *Geophysical Research Letters*, **44 (4)**, 1848–1856, https://doi.org/https://doi.org/10.1002/2016GL071515, URL https://doi.org/10.1002/2016GL071515.

Palmer, P. I., and Coauthors, 2023: Drivers and impacts of Eastern African rainfall variability. *Nature Reviews Earth & Environment*, **4 (4)**, 254–270, https://doi.org/10.1038/s43017-023-00397-x, URL https://doi.org/10.1038/s43017-023-00397-x.

Pomposi, C., C. Funk, S. Shukla, L. Harrison, and T. Magadzire, 2018: Distinguishing southern Africa precipitation response by strength of El Niño events and implications for decision-making. *Environmental Research Letters*, **13 (7)**, 074 015, https://doi.org/10.1088/1748-9326/aacc4c, URL https://dx.doi.org/10.1088/1748-9326/aacc4c.

Power, S., M. Haylock, R. Colman, and X. Wang, 2006: The Predictability of Interdecadal Changes in ENSO Activity and ENSO Teleconnections. *Journal of Climate*, **19 (19)**, 4755–4771, https://doi.org/https://doi.org/10.1175/JCLI3868.1, URL https://journals.ametsoc.org/view/journals/clim/19/19/jcli3868.1.xml.

Rodrigues, R. R., R. J. Haarsma, E. J. D. Campos, and T. Ambrizzi, 2011: The Impacts of Inter–El Niño Variability on the Tropical Atlantic and Northeast Brazil Climate. *Journal of Climate*, **24 (13)**, 3402–3422, https://doi.org/https://doi.org/10.1175/2011JCLI3983.1, URL https://journals.ametsoc.org/view/journals/clim/24/13/2011jcli3983.1.xml.

Ross, K. W., M. E. Brown, J. P. Verdin, and L. W. Underwood, 2009: Review of FEWS NET biophysical monitoring requirements. *Environmental Research Letters*, **4 (2)**, 024 009, https://doi.org/10.1088/1748-9326/4/2/024009, URL https://dx.doi.org/10.1088/1748-9326/4/2/024009.

Saji, N. H., B. N. Goswami, P. N. Vinayachandran, and T. Yamagata, 1999: A dipole mode in the tropical Indian Ocean. *Nature*, **401 (6751)**, 360–363, https://doi.org/10.1038/43854, URL https://doi.org/10.1038/43854.

Saji, N. H., and T. Yamagata, 2003: Possible impacts of Indian Ocean Dipole mode events on global climate. *Climate Research*, **25 (2)**, 151–169, URL https://www.int-res.com/abstracts/cr/v25/n2/p151-169.

Sazib, N., l. E. Mladenova, and J. D. Bolten, 2020: Assessing the Impact of ENSO on Agriculture Over Africa Using Earth Observation Data. *Frontiers in Sustainable Food Systems*, **4**, https://doi.org/10.3389/fsufs.2020.509914, URL https://www.frontiersin.org/articles/10.3389/fsufs.2020.509914.

Scanlon, B. R., and Coauthors, 2022: Linkages between GRACE water storage, hydrologic extremes, and climate teleconnections in major African aquifers. *Environmental Research Letters*, **17 (1)**, 014 046, https://doi.org/10.1088/1748-9326/ac3bfc, URL https://dx.doi.org/10.1088/1748-9326/ac3bfc.

Schneider, U., S. Hänsel, P. Finger, E. Rustemeier, and M. Ziese, 2022: GPCC Full Data Monthly Product Version 2022 at 0.25 °: Monthly Land-Surface Precipitation from Rain-Gauges built on GTS-based and Historical Data. *Global Precipitation Climatology Centre (GPCC) at Deutscher Wetterdienst*, https://doi.org/10.5676/DWD_GPCC/FD_M_V2022_025.

Taschetto, A. S., C. C. Ummenhofer, M. F. Stuecker, D. Dommenget, K. Ashok, R. R. Rodrigues, and S.-W. Yeh, 2020: *ENSO Atmospheric Teleconnections*, 309–335. Geophysical

Monograph Series, https://doi.org/https://doi.org/10.1002/9781119548164.ch14, URL https://doi.org/10.1002/9781119548164.ch14.

Ubilava, D., and M. Abdolrahimi, 2019: The El Niño impact on maize yields is amplified in lower income teleconnected countries. *Environmental Research Letters*, **14 (5)**, 054 008, https://doi.org/10.1088/1748-9326/ab0cd0, URL https://dx.doi.org/10.1088/1748-9326/ab0cd0.

Vashisht, A., B. Zaitchik, and A. Gnanadesikan, 2021: ENSO Teleconnection to Eastern African Summer Rainfall in Global Climate Models: Role of the Tropical Easterly Jet. *Journal of Climate*, **34 (1)**, 293–312, https://doi.org/https://doi.org/10.1175/JCLI-D-20-0222.1, URL https://journals.ametsoc.org/view/journals/clim/34/1/JCLI-D-20-0222.1.xml.

Vimont, D. J., M. Newman, D. S. Battisti, and S.-I. Shin, 2022: The Role of Seasonality and the ENSO Mode in Central and East Pacific ENSO Growth and Evolution. *Journal of Climate*, **35 (11)**, 3195–3209, https://doi.org/https://doi.org/10.1175/JCLI-D-21-0599.1, URL https://journals.ametsoc.org/view/journals/clim/35/11/JCLI-D-21-0599.1.xml.

Webster, P. J., A. M. Moore, J. P. Loschnigg, and R. R. Leben, 1999: Coupled ocean–atmosphere dynamics in the Indian Ocean during 1997–98. *Nature*, **401 (6751)**, 356–360, https://doi.org/10.1038/43848, URL https://doi.org/10.1038/43848.

Yeh, S.-W., and Coauthors, 2018: ENSO Atmospheric Teleconnections and Their Response to Greenhouse Gas Forcing. *Reviews of Geophysics*, **56 (1)**, 185–206, https://doi.org/https://doi.org/10.1002/2017RG000568, URL https://doi.org/10.1002/2017RG000568.